UNIVERSITY OF OKLAHOMA

GRADUATE COLLEGE

# APPLICATIONS OF DIATOMIC MOLECULES

A DISSERTATION

SUBMITTED TO THE GRADUATE FACULTY

in partial fulfillment of the requirements for the

Degree of

DOCTOR OF PHILOSOPHY

By

JAMES COKER
Norman, Oklahoma
2015

# Applications of Diatomic Molecules

A Dissertation Approved for the
Homer L. Dodge Department of Physics and Astronomy

By

Dr. John Moore-Furneaux, Chair

Dr. Gregory Parker

Dr. Eric Abraham

Dr. Phillip Gutierrez

Dr. Keri Kornelson

To my wife, Aimee, and my four wonderful children.

# Table of Contents

# List of Tables

# List of Figures

# Abstract

I present a study and application of diatomic molecules to various uses in the laboratory. It begins with an experiment to trap ultracold nitric oxide, then proceeds to multiple experiments where tellurium is utilized to create a frequency-stable laser system, and concludes with a spectroscopic study of $^{130}Te_2$ itself. While all of these experiments are quite different, they share at their core the fact that diatomics have a complex and interesting energy structure. Each experiment is aimed to exploit uniquely diatomic features.

## Chapter 1

# Introduction

Diatomic molecules are molecules made of two atoms, but simply combining one atom with another dramatically changes the energy structure of the system. With two cores, this new object has two extra degrees of freedom: rotation and vibration. Isotropic symmetry is lost as the internuclear axis is introduced and necessitates a rewrite in notation. Concepts of angular momentum can't be treated without considering their projection onto this new axis. These complications make them interesting though, as diatomic molecules exhibit properties that can be exploited for useful measurements. Enhanced sensitivity to the fine-structure constant [1], the electric dipole moment of the electron [2], and parity violation [3] have been observed, for example, and they've even been used to study Fermi gases [4].

Here we primarily discuss their interactions with lasers and their optical spectra. The following chapter is about the attempt to optically pump and trap nitric oxide for ultracold studies. Nitric oxide (NO) has piqued the interest of biologists [5], nutritionists [6], chemists [7], physicists [8], and environmental scientists [9] alike. The ability to trap and study it in ultracold conditions would be beneficial and applicable to many fields as well as ultracold science itself.

In this experiment we begin with NO at a temperature around 2-20 K. We attempt to achieve ultracold temperatures by taking advantage of its magnetic dipole moment, and trapping it with a permanent magnet setup. At the source temperature, all the

population is in a state that has zero magnetic dipole moment, so the initial challenge is to optically pump NO into the desired state. The trap and its details are the subject of P. Dahal's thesis [10], but the preliminary work setting up that experiment is detailed here in Chapter 2.

Following the NO experiment are two chapters concerning diatomic tellurium ($^{130}Te_2$). Tellurium is a heavy mineral discovered in 1782 [11] with no biological function, except that it's mildly toxic [12]. Why physicists find it of use however, is that it has tens of thousands of optical transitions spanning the blue part of the visible spectrum. With a line density of about 1 line every 1 GHz it can be a nightmare to spectroscopists but a boon to metrologists. Similar to iodine, it has been widely used as a frequency reference for this reason [13, 14, 15, 16].

In chapter 3 tellurium is used as a frequency standard to demonstrate the precision of stable laser systems. The first system takes advantage of the dispersion of nitrogen gas [17] and its linear dependence on pressure. As we are able to control the pressure of Nitrogen gas in a linear fashion, we are able to control its dispersion in a linear fashion. We demonstrate a setup where a stabilized HeNe laser (reference) and a blue diode laser (target) are simultaneous resonant with a single, nitrogen filled, Fabry-Pérot cavity. As we tune the dispersion, they remain simultaneously resonant while the target laser is being scanned, and thuse we have cavity dispersion tuning spectroscopy (CDT). With this setup we measure a few tellurium transitions and compare with work done by others. The work was published in the *Journal of the Optical Society of America B* in 2011.

Following that a series of improvements are detailed which radically alter the system. We achieve much greater stability and tunability. The new setup is demonstrated by taking precise measurements of over 9000 optical transitions of $^{130}Te_2$, and the system is characterized using a cesium frequency standard to make Allan deviation measurements.

The final chapter is about $^{130}Te_2$ and its properties. The measurement of 9000 transitions was useful as an atlas of references, but it didn't stop there. With all this data we were able to assign over 1400 lines to rotational and vibrational states. Using this information, we deduce spectroscopic properties of $^{130}Te_2$ to unprecedented precision. In addition we discuss the Morse Long Range potential (MLR) [18] and its usefulness for studying heavy diatomics. This new formulation of potential curves of diatomic molecules has major advantages over the polynomial Dunham model from the 1930's [19]. It has been used to advance our understanding of other diatomic potentials [20, 21], and we now apply it to $^{130}Te_2$ to develop a more accurate potential and gain new understanding of its properties.

Diatomic molecules have a wide variety of applications in physics and other sciences. What I present here is mostly a pure study of diatomic molecules themselves, but also the application to stable laser systems. We now turn our attention to an experiment involving ultracold nitric oxide.

# Chapter 2

# Generation of Ultraviolet Light and the Preparation for Optical Pumping of Nitric Oxide

## 2.1 Background and Outline of the Experiment

Ultracold molecules are of interest to a wide variety of research groups today [22]. Current applications include, but are not limited to: controlled chemistry [23], collision studies [24], and the development of quantum computing [25]. Although the field of cooling molecules has developed for decades, the work has been mostly limited to alkali metals [26]. We are interested in trapping Nitric Oxide (NO), which at present has not been done successfully anywhere. NO is a significant molecule for the chemistry of life on earth, capturing the interests of Biologists, Chemists, and Physicists alike [27, 28, 29]

Nitric Oxide, in its ground electronic state, to a good approximation, is a Hund's case (a) molecule [30]. This means that the electronic orbital motion and spin are strongly coupled to the internuclear axis, and not to the nuclear rotation. The ground state of NO is a $^2\Pi$ doublet, with the lower $^2\Pi_{1/2}$ and upper $^2\Pi_{3/2}$ states separated by $\sim$ 120 cm$^{-1}$ [31]. In the $^2\Pi_{1/2}$ state, the magnetic moments due to the orbital and spin angular momenta cancel, but in the $^2\Pi_{3/2}$ they combine to yield a magnetic moment of $\sim$ 2 $\mu_B$. The $^2\Pi_{3/2}$ states of NO are thus paramagnetic, and could in principle be trapped by an appropriately designed permanent magnetic trap.

In our experiment, the NO source is at a temperature of around 2-20 K. At this

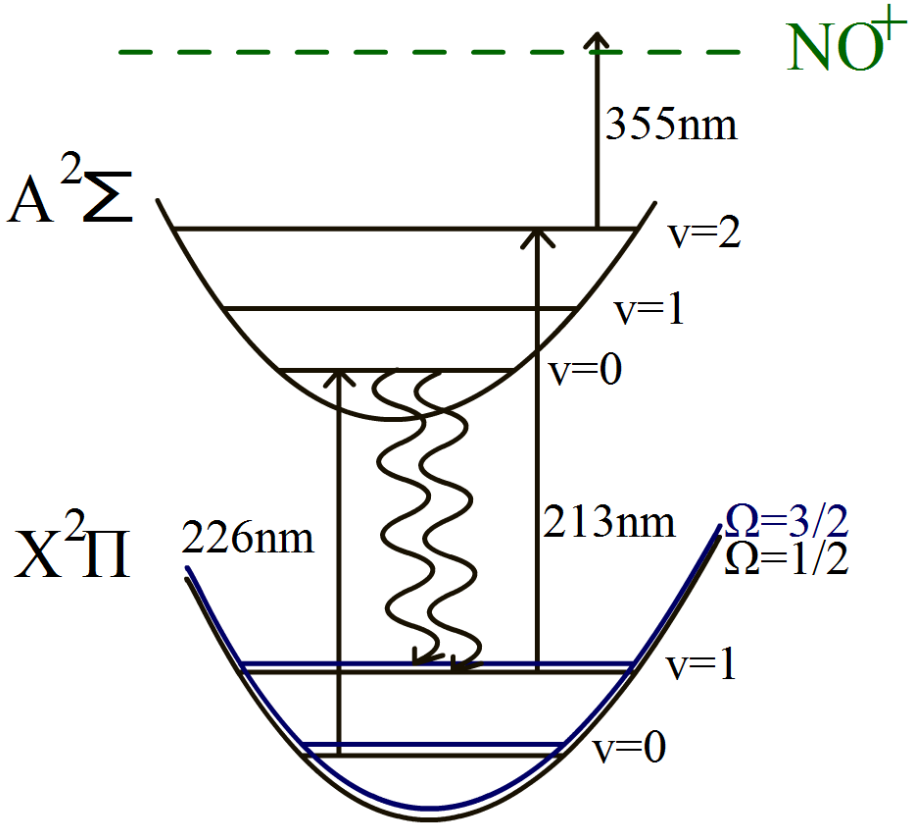


Figure 2.1: The optical pumping scheme and detection scheme. The wavelengths of the three lasers used are labeled. The second step is a spontaneous fluorescence to both $\Omega$ states with $v = 1$.

temperature the population ratio for $^2\Pi_{3/2}$ to $^2\Pi_{1/2}$ is less than $10^{-7}$. To increase this trap's density, minimizing the population of the $^2\Pi_{1/2}$ state is desired, because it has a zero magnetic moment. For this reason we wish to optically pump NO out of this state. The pumping scheme is shown in Fig. 2.1. We wish to drive the $A_{v=0}\ ^2\Sigma \leftarrow X_{v=0}\ ^2\Pi_{1/2}$ transition with 226 nm light and allow the $A_{v=0}\ ^2\Sigma$ state to fluoresce down to the $X_{v=1}\ ^2\Pi_\Omega$ state, which will favor populating $\Omega = \frac{3}{2}$ over $\Omega = \frac{1}{2}$ because of its greater degeneracy. We would then drive the $A_{v=2}\ ^2\Sigma \leftarrow X_{v=1}\ ^2\Pi_\Omega$ transition for detection.

The final transition seen in Fig. 2.1 is the ionization required ($A_{v=2} \rightarrow NO^+$) for our detection method, which was resonance-enhanced multi-photon ionization (REMPI) [32, 33]. The 355 nm beam was made by tripling the frequency of a 1064 nm beam, as discussed in detail in the next section. For the experiment our 213 nm laser was tuned to look for $A_{v=2}\ ^2\Sigma \leftarrow X_{v=1}\ ^2\Pi_{1/2}$ initially as it would demonstrate that optical pumping had occurred all the same. If $X_{v=1}\ ^2\Pi_{1/2}$ had become noticeably populated it would be strong evidence that $X_{v=1}\ ^2\Pi_{3/2}$ was also populated. Before the 226 nm beam was set up, we scanned the area where $A_{v=2}\ ^2\Sigma \leftarrow X_{v=1}\ ^2\Pi_{1/2}$ transitions should be present and verified that it wasn't populated.

If optical pumping succeeds, we should see a dramatic increase in population of the $X_{v=1}$ state, be it $^2\Pi_{1/2}$ or $^2\Pi_{3/2}$. Initially, we also wanted to verify that the fluorescence $A_{v=0} \rightarrow X_{v=1}$ must have reasonable probability. The Franck-Condon factors previously measured for NO show that the fluorescence to $X_{v=1}$ (to either $\Omega = \frac{1}{2}$ or $\frac{3}{2}$) is the most probable from $A_{v=0}$, with a probability $\sim$ 30% [34]. Therefore we expect a significant increase in $X_{v=1}$ population when the 226 nm beam is included.

## 2.2 Creation of Ultraviolet Light Using Birefringent Crystals

Among various hurdles to overcome, there is the problem of generating ultraviolet (UV) light for this experiment. Research grade ultraviolet light sources are not common. Excimer lasers produce UV light, but only at certain specific wavelengths which are not tunable, and not of optical quality required for spectroscopy [35]. To overcome these issues, harmonic generation through birefringent crystals can be employed. At

this point I will digress for a quantitative description of frequency mixing in such crystals.

By applying Maxwell's equations for anisotropic media to incoming electromagnetic waves, an equation for the intensity of sum-frequency-generated (SFG) light produced is derived in Ref. [36]. Letting the subscripts 1, 2 and 3 refer to the two incident beams and the generated beam, respectively, and $I$, $n$ and $\lambda$ refer to the intensity, index of refraction, and wavelength, respectively, their result is:

$$I_3 = \frac{512\pi^5 d_{\text{eff}}^2 I_1 I_2}{n_1 n_2 n_3 \lambda_3^2 c} L^2 \text{sinc}^2(\Delta k L/2) \tag{2.1}$$

with

$$\Delta k \equiv k_1 + k_2 - k_3 \tag{2.2}$$

Here $d_{\text{eff}}$ is the nonlinear coefficient of the crystal, and $L$ is the length of the crystal. For the special case of second harmonic generation (SHG), one could simply assert that $n_1 = n_2$ and $I_1 = I_2$. For third harmonic generation (THG), one combines the original beam and generated beam from SHG for SFG. The energy level diagram in Fig. 2.2 demonstrates a simple model of this.

We now turn our attention to the question of how to achieve the most intensity for the generated light. The parameters in Eq. 2.1 which are most important to us[1] are the intensities of the incident beams $I_1$ and $I_2$, the condition at which the sinc function is maximized ($\Delta k L = 0$), and the nonlinear coefficient of the crystal $d_{\text{eff}}$.

The intensities of the incident beams are something we can control by focusing

[1]Indices of refraction will not vary much by choice of crystal, and a longer crystal length $L$ only makes the phase-matching condition worse, requiring more mechanical stability, and small perturbations would weaken the intensity.

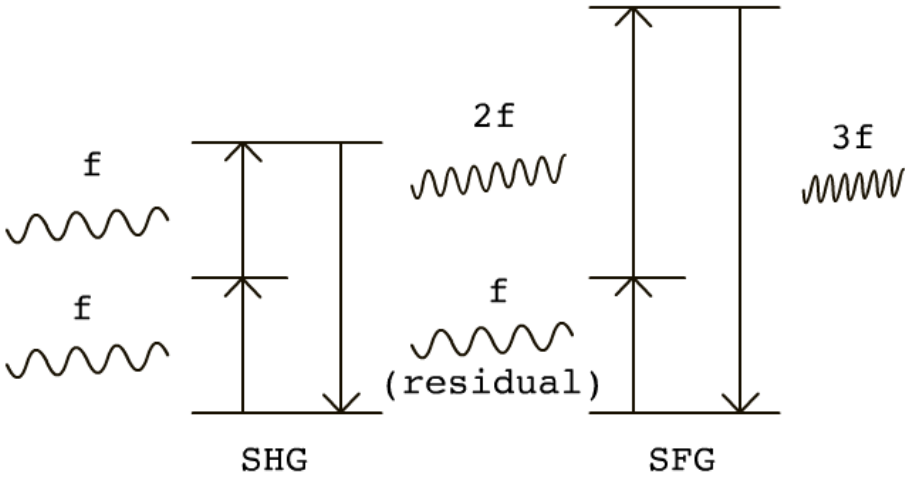


Figure 2.2: An energy level diagram representing third harmonic generation as a combination of second harmonic generation and sum-frequency generation.

the beam at the point of incidence with the crystal. This then makes it necessary to add a collimating lens after every focusing lens to prevent excessive divergence later in the beam path. The phase matching condition is achieved by careful control of temperature and angular orientation of the crystal. Two kinds of phase matching exist, dependent on the crystal. Type I requires the polarizations of the incident beams to match, and type II requires the polarizations to be perpendicular to each other. A summary of the properties of commonly used birefringent crystals is given in Table 2.1.

While Potassium titanyl phosphate (KTP) and Lithium niobate ($LiNbO_3$) have the largest $d_{\text{eff}}$, both require elevated temperatures for operation, and neither is transparent at the UV wavelengths we need. For these reasons, Potassium dideuterium phosphate (KD*P), Beta barium borate (BBO), and Lithium triborate (LBO) crystals were used.

| Material | Match. Type | $d_{\text{eff}}$ (pm/V) | Transp. Range (nm) | Ideal T ($^o$C) | $\Delta\theta$ (mrad) | $\Delta T$($^o$C) | $\Delta\lambda$ (nm) |
|---|---|---|---|---|---|---|---|
| KD*P | II | 0.38 | 200-2000 | 25 | 5.0 | 13 | 6.5 |
| KTP | II | 5.27 | 350-4500 | >65 | 15-68 | 25 | 0.56 |
| $LiNbO_3$ | I | 5.89 | 330-5500 | >170 | 3.1 | 1.1 | 0.3 |
| BBO | I | 2.01 | 200-2600 | 22 | 1.8 | 50 | 0.66 |
| LBO | I | 1.17 | 160-2600 | 25 | 70 | 5.8 | 4.37 |

Table 2.1: A summary of properties of some birefringent crystals. These numbers were found in Ref. [37]. The quantities $\Delta\theta$, $\Delta T$, and $\Delta\lambda$ are the angular bandwidth, temperature bandwidth, and wavelength bandwidth, respectively.

An additional bonus with these three crystals is the large temperature bandwidth, requiring no regulation of temperature beyond what the lab air conditioning system provides.

The 355 and 213 nm light were generated with a pulsed neodymium-doped yttrium aluminium garnet (Nd:YAG) laser (Quanta-Ray DCR3) and a dye laser (Lambda Physik Scanmate) using $C_{19}H_{17}N_3O$ dye (DCM). The experimental setup is shown in Fig. 2.3. The KD*P crystal near the Nd:YAG laser, which provides both SHG and THG, is attached to the laser. It was built inside a case with two knobs for fine-tuning two orientation angles of the crystal, which allow control of the relative intensities of the 532 and 355 nm light. A dichroic beam splitter directs the 532 nm beam toward the dye laser and the 355 nm beam towards the chamber. The 532 nm beam pumps the dye laser, which makes 639 nm light. The next two crystals provide THG, making 213 nm light. The 320 nm light from the KD*P crystal comes with a $\pi/2$ rotation

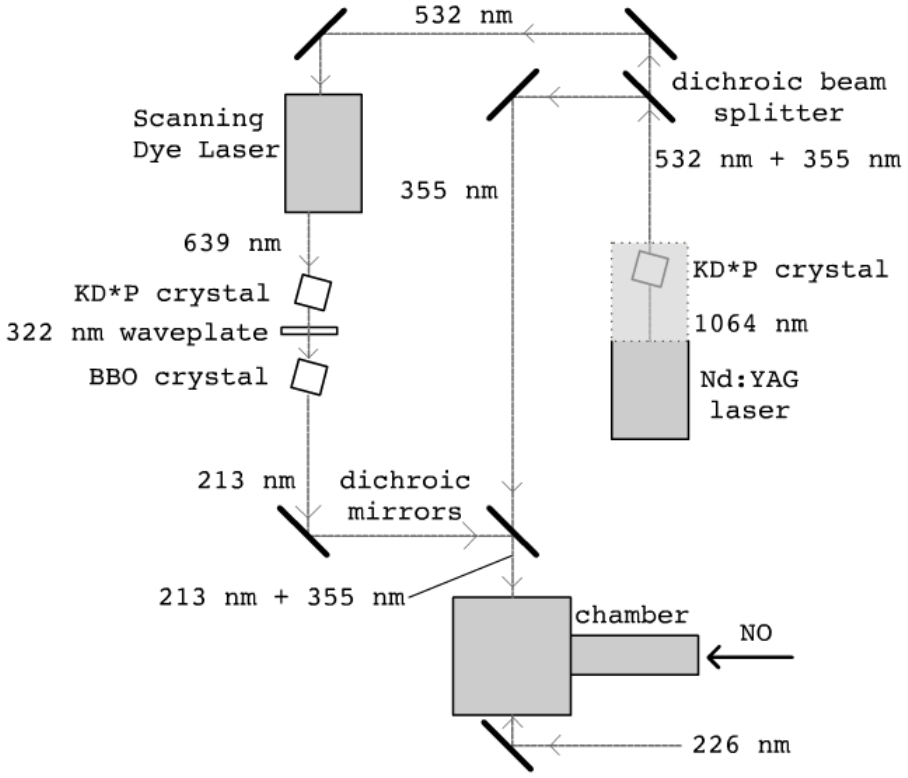


Figure 2.3: The experimental setup for optical pumping of NO. The generation of 226 nm light is described later in this section.

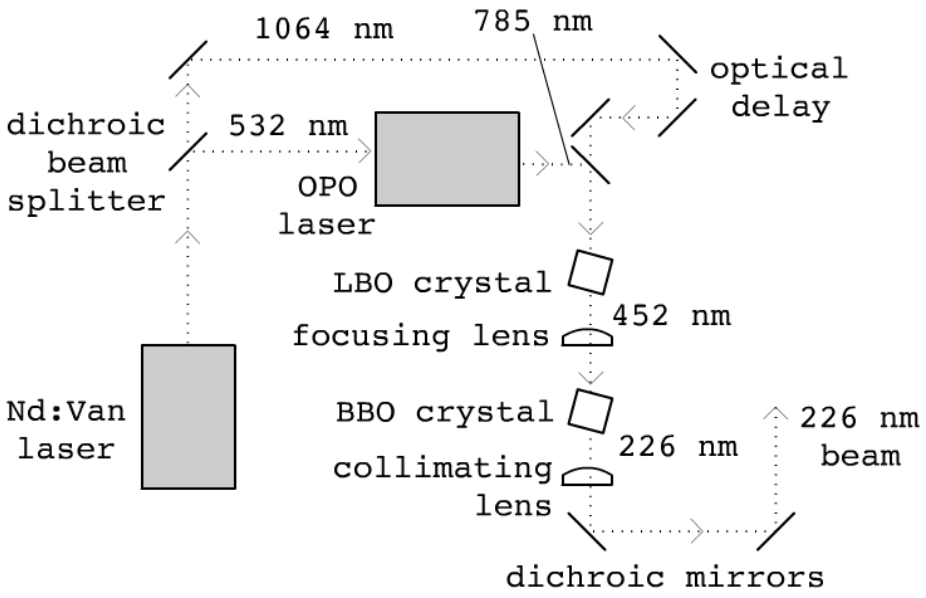


Figure 2.4: The setup used for generation of 226 nm light.

of its polarization, making it necessary to place a waveplate before the BBO crystal so that the polarizations of the 320 nm and 644 nm match. The dichroic mirrors after that filter out the undesired, residual harmonics. The 226 nm light is made from another laser system, which is described next.

To create ultraviolet light at 226 nm, we used a picosecond-neodymium-vanadate (Nd:Van) laser (brand and model) and an optical parametric oscillator (OPO) laser (brand and model). The setup used is shown in Fig. 2.4. The Nd:Van laser produces both 1064 and 532 nm light. A dichroic beam splitter directs the 532 nm light toward the OPO laser and the 1064 nm light towards the LBO crystal. The OPO laser produces 785 nm light which combines in the LBO crystal to make 452 nm light via SFG. The 452 nm light is then frequency-doubled in the BBO crystal via SHG. The lenses shown focus and collimate the beam. The dichroic mirrors filter out

| Wavelength (nm) | 532 | 639 | 213 | 355 | 1064 | 532 | 787 | 452 | 226 |
|---|---|---|---|---|---|---|---|---|---|
| Power (mW) | 1000 | 20 | 1.4 | 13 | 3600 | 3300 | 1200 | 730 | 34 |

Table 2.2: The measured power of every beam used in the experiment. The first four are from the setup of Fig. 2.3 and the last five are from the setup of Fig. 2.4

undesired residual harmonics. From conservation of energy, we have simple equations to determine what wavelength is made in the end:

$$\frac{1}{1064} + \frac{1}{785} \approx \frac{1}{452} \quad \text{(SFG)} \tag{2.3}$$

$$\frac{1}{452} + \frac{1}{452} = \frac{1}{226} \quad \text{(SHG)} \tag{2.4}$$

This is done by adding the photon energies $h\nu$, but dividing every term by $hc$.

The power of each isolated beam was measured, to monitor efficiency of harmonic generation. Table 2.2 shows all measured powers.

Thus, all the light needed was made. Before simulation of the optical pumping experiment was possible, we took spectra of NO.

## 2.3 Spectroscopy of Nitric Oxide

To calibrate the laser and demonstrate a functioning setup, we first took several spectra of NO. The experiment was setup as shown in Fig. 2.3, but without the 226 nm beam. The tuning range of the dye we used, DCM, is 605 to 725 nm [38]. We scanned from 639 nm to 645 nm, which after tripling the frequency becomes 213 nm to 215 nm. In

this region the transition $X^2\Pi_{\nu=0} \leftarrow A^2\Sigma_{\nu'=1}$ is found, and we simulated the spectra for comparison. Precise simulation of NO spectra across 3 nm of transitions required at least three considerations: calculating the energy levels, weighting the values with a Maxwell-Boltzmann distribution, and imaging the Gaussian beam at every point. The Hamiltonian used comes from Brown and Carrington [39] and the constants from Ref. [40]. For the A state the Hamiltonian is:

$$H_1^A = T_1^A + B_1^A(J+\frac{1}{2})(J+\frac{3}{2}) - D_1^A((J+\frac{1}{2})(J+\frac{3}{2}))^2 - \frac{q^A}{2}(1 \pm (J+\frac{1}{2})) \quad (2.5)$$

where $T_\nu^A$ is the vibrational band origin, $B_\nu^A$ is the rotational constant, $D_\nu^A$ is the centrifugal distortion constant, $q$ is the $e/f$ parity constant, $J$ is the rotational quantum number, the subscripts '1' refer to the $\nu' = 1$ vibrational state, and the superscripts 'A' refer to the excited A state of NO. For the ground state $X^2\Pi$ there is mixing between the $^2\Pi_{1/2}$ and $^2\Pi_{3/2}$ states, causing off-diagonal terms in the Hamiltonian:

$$\begin{aligned} H_0^X &= A_x \begin{bmatrix} 1/2 & 0 \\ 0 & -1/2 \end{bmatrix} + A_D \begin{bmatrix} x/2 & 0 \\ 0 & -x/2-1 \end{bmatrix} + B_0^X \begin{bmatrix} x & -\sqrt{x} \\ -\sqrt{x} & x+2 \end{bmatrix} \\ &+ D_0^X \begin{bmatrix} -x(x+1) & 2\sqrt{x}(x+1) \\ 2\sqrt{x}(x+1) & -(x+1)(x+4) \end{bmatrix} \pm p^X \begin{bmatrix} 0 & 0 \\ 0 & -(J+1/2)/2 \end{bmatrix} \\ &\pm q^X \begin{bmatrix} 0 & \sqrt{x}(J+1/2)/2 \\ \sqrt{x}(J+1/2)/2 & -(J+1/2) \end{bmatrix} \end{aligned} \quad (2.6)$$

where $A_X$ and $A_D$ are associated with the difference between $^2\Pi_{1/2}$ and $^2\Pi_{3/2}$, $B_0^X$ and $D_0^X$ are the rotational and distortion constants for the ground state with $\nu = 0$,

$p^X$ and $q^X$ are the $e/f$ parity constants, and $x \equiv (J-1/2)(J+3/2)$. Using these Hamiltonians I was able to generate the optical transition energies we expected to see around 213 to 215 nm. Applying rotational degeneracy and the Maxwell-Boltzmann distribution, I calculated weights for all transitions:

$$w(J, E_X) = (2J+1)e^{-E_X/k_BT} \tag{2.7}$$

where $E_X$ is the ground state energy and $T$ was fixed at room temperature. With a list of energies and probabilities, the next step was to apply the laser's Gaussian frequency distribution with the appropriate width. The frequency width of the laser was measured to be about 0.0025 nm. For every expected transition a Gaussian model was generated with the modeled position and intensity, and with the laser's width. They were then summed to create the simulated spectra. In comparison to the measured data, we were able to match the data and therefore calibrate the laser to about 0.002 nm. A sample of this match is depicted in Fig. 2.5, where the simulated spectra is depicted upside-down.

## 2.4 Optical Pumping of Nitric Oxide

With a source of 226 nm light and a functioning NO measurement setup, we were ready to start preliminary experiments towards optical pumping. In Mathematica I simulated this experiment first. This simulation had three parts: populating the $A_{\nu'=0}$ state, fluorescence to the $X_{\nu''=1}$ state, and optical transition to the $A_{\nu'''=2}$ state. The first part was similar to the NO spectra simulation: calculate what $X_{\nu=0} \leftarrow A_{\nu'=0}$

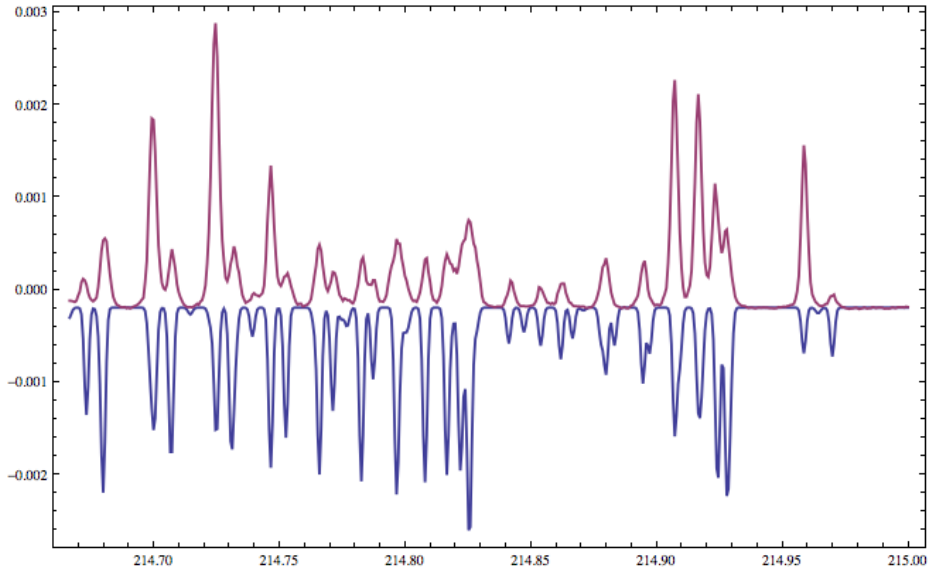


Figure 2.5: Nitric Oxide spectra atop simulated spectra (arb. vs nm)

transitions exist in the region, apply weighting according to rotational degeneracy and the Maxwell Boltzmann distribution, and apply the Gaussian beam profile. For the second part we considered the Franck-Condon factors for the $A_{\nu'=0} \rightarrow X_{\nu''=1}$ fluorescence, which sources [34, 40, 41, 42, 43] show to be about 30%. The intensities at that stage were calculated assuming each relaxation would be of $\Delta J = 0, \pm 1$ [39] and that all three branches were of equal probability. From there, the third part is done just as the first, but instead of using rotational degeneracy and the Maxwell-Boltzmann distribution to calculate the weights, the intensities from the second part were used. A two-dimensional plot depicting this simulation is given in Fig. 2.6, where the two controlled axes refer to the wavelengths of the dye laser and the OPO laser used. Results of optically pumping NO are presented in Parshuram Dahal's dissertation [10].

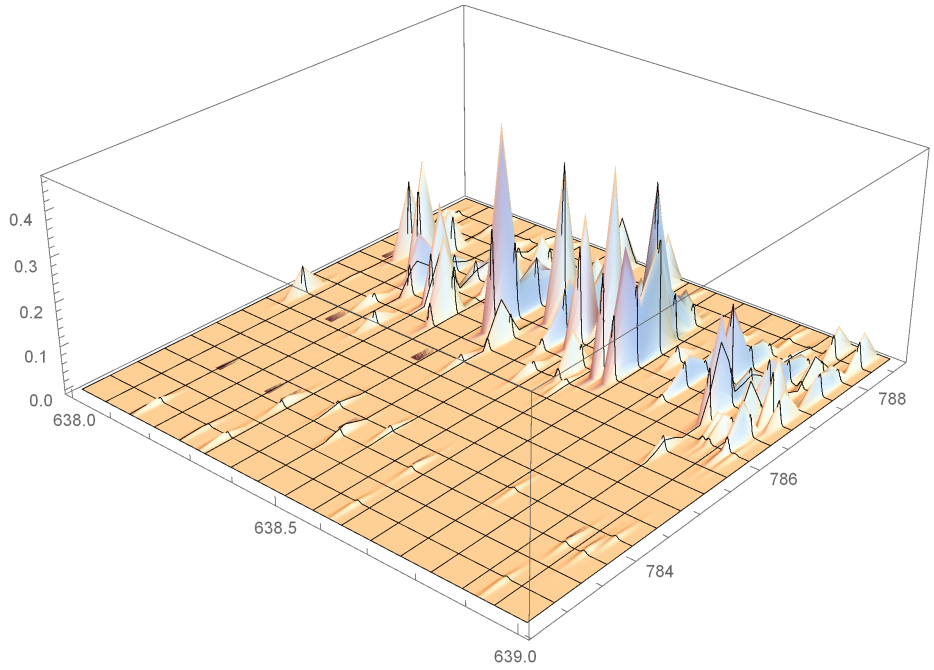


Figure 2.6: Predicted relative intensities measured in optical pumping experiment as two lasers are scanned (arb. vs nm vs nm)

# Chapter 3

# Developing a Stable, Tunable, Repeatable Frequency Source near 440 nm

## 3.1 Introduction

At this point we turn our attention to a different diatomic molecule: tellurium ($Te_2$). In preparation for an experiment to measure the electric dipole moment of the electron using PbF proposed by Neil Shafer-Ray in 2006 [44], a stable frequency source was needed in the vicinity of 440 nm. It needed to be locked with a drift of under few MHz (or $1 : 10^9 \Delta f/f$) over several hours, and the ability to scan a GHz or more in a reliable fashion. Tellurium was known to have been used as a frequency reference with transitions in this region [13, 45], so we setup a tellurium cell and began to work to improve our laser.

The first method we implemented was cavity dispersion tuning [46]. With this method, a helium-neon reference laser (632.8 nm) is locked to an optical cavity filled with nitrogen gas, and the pressure of the nitrogen gas is adjusted until our diode laser (440 nm) can be locked simultaneously. At this point, when the $N_2$ pressure is changed, the frequency of the laser near 440 nm will sweep due to the dispersion of the $N_2$. We characterized this method by exploring some $^{130}Te_2$ transitions and published the results in the *Journal for the Optical Society of America B*. Next, that paper is reproduced to present this result.

## 3.2 Cavity Dispersion Tuning Spectroscopy of Tellurium Near 444.4 nm

### 3.2.1 Introduction

The diode laser has been a valuable research tool since the 1960's [47, 48]. Though it has been used for countless experiments over the decades, many applications require frequency stability beyond that provided by typical commercial mode-locked systems. An unaided, research grade diode laser typically drifts from several MHz/min to a few MHz/hr [49]. A handful of techniques have arisen over the years to improve the frequency stability of diode lasers.

One method is to feedback stabilize the laser frequency to an atomic absorption or fluorescence line. For example, the setup of Ref. [50] used a GaAlAs laser, with a 3.0 kHz frequency modulation, to create fluorescence from a well known transition in cesium. If the laser were tuned slightly below the peak (to the red), then the 3.0 kHz modulation would be seen in the fluorescence signal, in phase with the modulation that was written on the laser. If the laser were tuned slightly above the peak (to the blue), then the 3.0 kHz modulation would be seen in the fluorescence signal with opposite phase. By use of a lock-in amplifier, an error signal was generated, appropriately amplified, and fed back to the current controller of the laser diode. With this setup, a frequency drift of $< 50$ kHz was demonstrated. While the improvement of frequency stability by 3 to 5 orders of magnitude is impressive, the experimenter is limited by

having to lock at a specific, well-known transition.

Another method, the Dichroic-Atomic-Vapor Laser Lock (DAVLL), engineers the error signal by Zeeman splitting an atomic transition and subtracting the two Doppler-broadened peaks [51]. In the atomic vapor cell, circularly polarized light of one direction absorbs at energies shifted downward while circularly polarized light of the opposite direction absorbs at energies shifted upward. By passing through a $\lambda/4$ waveplate and a polarization beam splitter after the cell, the two polarizations can be detected separately and their signals subtracted to produce an error signal. Rotating the $\lambda/4$ waveplate and adjusting the magnetic field give convenient tuning parameters, allowing for a scanning range around 500 MHz. The frequency stability of this method is typically $< 500$ kHz over a few days, and the recapture range is larger than ordinary line locking, but once again the experimenter is limited to a frequency range within $\sim 500$ MHz of a suitable optical transition.

A third method, referred to as a scanning transfer cavity lock, writes the stability of one laser onto another by keeping the time-difference in transmission of the two lasers through a sweeping etalon fixed using feedback electronics [52]. This fixed time-difference can then be controlled, allowing the locked laser to scan. This lock can have excellent long-term stability. Furthermore, the experimenter is no longer limited to lock frequencies close to a suitable atomic transition. However, the duty cycle for feedback is of the order of the cavity finesse ($\sim 1/100$), which limits the short term frequency stabilization of the lock.

We present a stabilization technique in which the laser is stable within 2 MHz

over several days and is capable of scanning over 400 MHz while locked. With a duty cycle of 100% and no mechanical oscillation necessary for feedback, the feedback rate could easily exceed 1 MHz. We demonstrate this setup by measuring Lorentzian line profiles and line spacings of optical transitions in molecular tellurium ($Te_2$) by saturation absorption spectroscopy. We discuss stability with time and temperature, and comment on the dispersions of Nitrogen and Carbon Dioxide gases.

### 3.2.2 Experimental Setup

The setup is described as three separate parts: the laser system, the physical principles of the locking and scanning system, and the optical setup for observation of saturated absorption lines in $Te_2$.

#### The Laser Locking System

The laser setup is depicted in Fig. 3.1. The Zeeman-stabilized HeNe laser (MicroGauss) is used as a reference for both a Wavemeter (Burleigh WA-1000) and a Fabry-Pérot (FP) Etalon (Toptica FPI100). The blue diode laser (Toptica SHG Pro) makes its 440 nm light by doubling 880 nm infrared (IR) light in a bow-tie cavity with a beta-barium-borate crystal. We control the frequency of the IR diode by adjusting both the diode current and the position of the grating in the external cavity. This frequency is then monitored with the wavemeter as shown in Fig. 3.1. The blue output is about 280 mW. A half-wave plate and a polarizing beam splitter is used to direct $\sim 30\%$ of this power to a $Te_2$ absorption cell and a beam splitter directs $\sim 1\%$ to the

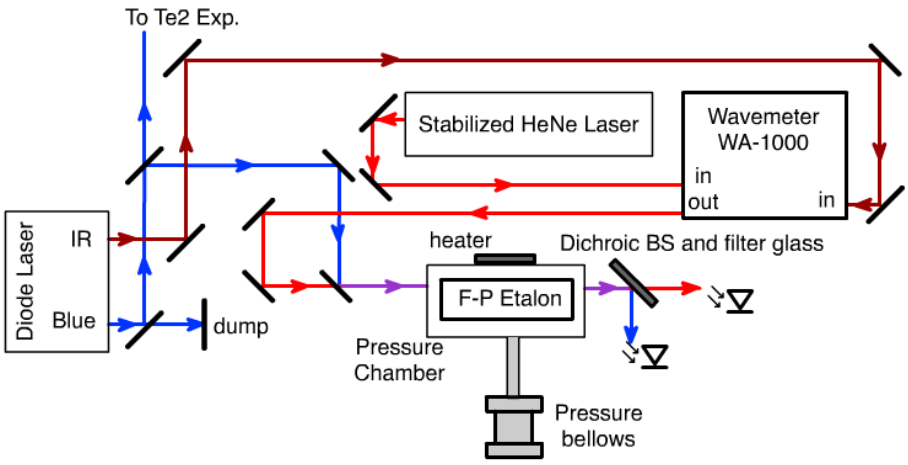


Figure 3.1: The laser locking system. The FP etalon is fixed inside a pressure chamber. Both the HeNe laser and the blue diode laser are resonant with the etalon, and after filtering optics each one is seen on its own photodiode.

etalon. The etalon temperature is controlled using a heater, and the etalon pressure is controlled using a stepper motor attached to bellows. The length of the etalon is controlled by shifting one of the mirrors with a piezoelectric transducer (PZT).

A combination of dichroic beam splitters and filter glass at the output of the etalon allows independent detection of the red and blue light at separate photodiodes. These signals are used for the electronic feedback loops. In contrast to the scanning transfer cavity system [52], for the duration of its lock, the FP cavity is continuously in resonance with both lasers. The FP cavity optical path is maintained in resonance with the HeNe laser as the index of refraction of the $N_2$ gas changes by adjusting the PZT on one of the mirrors. The mirror position is modulated at 5 kHz. If the response on the HeNe photodiode is in phase the cavity is shortened, and if the response is

$180^o$ out of phase the cavity is lengthened. The 5 kHz modulation and the error signal are added together in a transformer and applied to the PZT. This same modulation of the FP cavity also affects the reading from the blue laser's photodiode. This is similarly used to adjust the diode laser's frequency to maintain resonance with the FP cavity. This frequency is tuned by adjusting the grating and current of the diode laser system using the feed-forward grating control of the Toptica system.

Low pass filters are used for each of the error signals, and the optimal cutoff frequencies empirically found for each give a good estimate of the bandwidth of each lock. The cavity's lock to the reference laser is $\sim 500$ Hz, and that of the diode laser's lock to the cavity is $\sim 50$ Hz. The short term stability of the reference HeNe laser is reported by its documentation to be $< 100$ kHz. Here follows the theory of the locking system and dispersion tuning technique.

**Physics of Cavity Dispersion Tuning Spectroscopy**

By locking the cavity length $L$ to the HeNe reference laser wavelength $\lambda_R$, we set

$$L = \frac{\lambda_R}{2} N_R = \frac{c}{2 f_R n_R} N_R \tag{3.1}$$

for some fixed integer $N_R$, where $f_R$ and $n_R$ are the frequency and index of refraction of the reference laser and $c$ is the speed of light. By locking the blue diode laser vacuum wavelength $\lambda$ to the cavity the diode laser wavelength is set to

$$L = \frac{\lambda}{2} N = \frac{c}{2 f n} N \tag{3.2}$$

for some fixed integer $N$, where $f$ and $n$ are the frequency and index of refraction of the blue laser. The lock condition is therefore given by

$$\frac{nf}{n_R f_R} = \frac{N_R}{N} = \text{ A constant.} \tag{3.3}$$

The frequency $f$ changes to maintain this condition as $n$ and $n_R$ are altered. The etalon is filled with Nitrogen ($N_2$) gas, and the temperature $T$ and pressure $P$ are controlled with a heater and bellows as mentioned above. At fixed $P_0 = 760$ torr and $T_0 = 15^o$ C, the index of refraction for different colors of visible light has been well characterized [17] :

$$\begin{aligned} n(P_0, T_0) - 1 &= \left(6497.378 + \frac{3073864.9}{144 - k^2}\right)/10^8 \\ &\equiv \alpha_0(k) \end{aligned} \tag{3.4}$$

where $k$ is the wavenumber of light in inverse microns. The values for the reference HeNe laser at 632.8 nm and the blue diode laser at 444.4 nm are $\alpha_0(k_R) = 2.8220 \times 10^{-4}$ and $\alpha_0(k) = 2.8622 \times 10^{-4}$, respectively. The index of refraction at a pressure and temperature $(P_f, T_f)$ may be related to the index of refraction at $(P_i, T_i)$ by the expression:

$$n(P_f, T_f) - 1 = \alpha_i(k)\Gamma_i^f \tag{3.5}$$

where, from Ref. [53]:

$$\Gamma_i^f = \frac{(P_f/T_f)Z_i}{(P_i/T_i)Z_f + \alpha_i Z_i(P_i/T_i - P_f/T_f)/6} \approx \frac{P_f}{T_f}/\frac{P_i}{T_i} \tag{3.6}$$

with

$$Z = 1 + \frac{P(T - 317.6 \text{ K}) \times 10^{-5}}{760 \text{ torr}} \tag{3.7}$$

being the compressibility of Nitrogen at a given $(P, T)$.

With $nf/n_R f_R$ a constant of the lock (Eq. 3.3), we derive an expression for the change in frequency of the tuned laser as the pressure and temperature are changed from $P_i, T_i$ to $P_f, T_f$:

$$\Delta f(P_f, T_f) = \frac{(\Gamma_0^f - \Gamma_0^i)(\alpha_0(k_R) - \alpha_0(k))}{(1 + \alpha_0(k_R)\Gamma_0^i)(1 + \Gamma_0^f \alpha_0(k))} f_i. \tag{3.8}$$

Here the subscript 0 denotes the $(P, T)$ conditions where the $\alpha$'s were measured in Ref. [17] and the $i$'s denote chosen reference frequency conditions.

**Optical Setup for Saturation Absorption Spectroscopy of Tellurium**

The optical setup surrounding the tellurium cell is illustrated in Fig. 3.2. Continuing from Fig. 3.1, the blue diode laser goes through a half-wave plate and a polarizing beam splitting cube (PBSC), splitting the beam in two, with the ratio of powers controllable by rotating the half-wave plate. The undeflected and deflected beams will be referred to as the pump and probe beams, respectively. The pump beam's intensity is made to oscillate by the electro-optical amplitude modulator (EOAM), which, in combination with wave plates B and C and the second PBSC, creates an electro-optical chopper. The pump beam passes through the third PBSC and is then detected by the photodiode. The probe beam is bent by all three PBSCs and detected by the other photodiode in the diagram. For the moment we will ignore the electrical-optical phase modulator (EOM*), as it was only used for part of the experiment described later in this paper.

The modulation source and the probe photodiode signal are fed into a lock-in

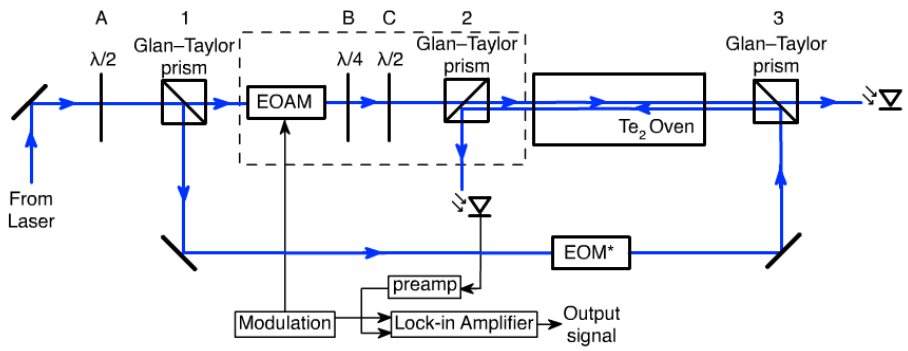


Figure 3.2: The optics surrounding the tellurium cell, which is held at $650^o$ C. The dashed box groups together the components that serve as an electro-optical chopper.

amplifier. While tuned to a tellurium line, the modulation of the pump beam becomes written on the probe beam. At a moment when the pump beam is of high intensity, a hole in the population is made, allowing more of the probe beam to pass. At a moment when the pump beam is of low intensity, the probe beam absorbs, allowing less of the probe beam to pass. The ideal modulation frequency should be set high to optimize the signal to noise ratio, but not high enough to distort relative peak intensities. We used a 40 kHz modulation.

### 3.2.3 Data

All peaks observed are from various rovibrational transitions in the $X_1(^3\Sigma_g) \leftarrow B_1(^3\Sigma_u)$ band, previously assigned line numbers in Ref. [13].

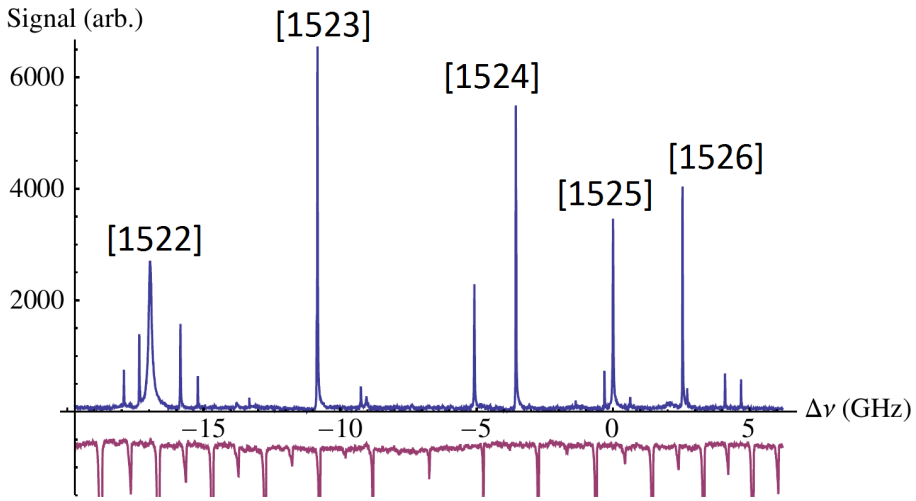


Figure 3.3: The preliminary diode laser grating scan, accurate to 50 MHz. The $x$-axis is the frequency displacement from 674611.02 GHz. The downward spikes are 1 GHz "markers" seen through the etalon. Some of the markers can't be seen at this scale.

### Preliminary Grating Scan

Initially, a scan of the PZT voltage on the diode laser's grating was performed over about 25 GHz. While scanning the grating, the etalon was locked to the HeNe, and the blue diode laser's intensity through the etalon was recorded. Spikes in intensity occurred when the frequency of the blue laser was resonant with the etalon, and they provided markers that indicate one free spectral range (FSR) in frequency. Our etalon is designed such that 1 FSR = 1 GHz, accurate to 1%. Our wavemeter was calibrated by an unrelated Rubidium experiment in a nearby lab, and found to be accurate to $< 1$ GHz. This scan is shown in Fig. 3.3.

Because stable scanning of the diode laser grating over a long frequency range

requires adjustment of the diode current, the scan is non-linear in frequency. After analysis, fitting a function to the GHz markers and rescaling, we can determine the intervals between lines to an uncertainty of 50 MHz. In matching our lines to Ref. [13], we define our line matching their line 1525 to be zero Hz and report the intervals measured in Table 3.1. We have full-width at half maximum (FWHM) values around 15 MHz, compared to the 3 GHz values of the previous work, so it is no surprise that we find 13 lines in the space where 5 were reported in Ref. [13].

**Cavity Dispersion Tuning Scan**

A Cavity Dispersion Tuning (CDT) scan consists of collection of saturated absorption spectra while regulating the cavity temperature to vary $< 0.03^o$ C and scanning the pressure by changing the volume of the closed chamber with a stepper motor driven bellows system. In principle, the frequency shift of each pressure point can be determined from Eq. 3.8. In practice, the limited gas purity and accuracy of the pressure gauge do not allow for that level of precision. For this reason 80.00000 MHz side-bands were added to the probe beam in some of the scans. These side-bands were then used to create an effective frequency calibration. The intensity of the diode laser through the FP cavity was monitored as data was taken, to confirm that the laser never lost lock. The intensity of the pump beam was also monitored, and its fluctuations found to be $< 10\%$.

The data indicates an interval of $289 \pm 3$ MHz, as seen in table 1. The FWHM values of the lines at -289 and 0 MHz measure 11 and 20 MHz, respectively. The

| Line position and previous assignment from Ref. [13] (GHz) | Interval from line 1525 found in this work (GHz) |
|---|---|
| 674594.113 [1522] | -17.92<br>-17.36<br>-16.97<br>-15.85<br>-15.21 |
| 674600.346 [1523] | -10.83 |
| 674607.751 [1524] | -5.08<br>-3.56 |
| 674611.022 [1525] | -0.289 ±0.003<br>0 |
| 674613.621 [1526] | 2.54<br>4.10<br>4.69 |

Table 3.1: Our reported intervals and those of Ref. [13]. All non-zero intervals have an uncertainty of 50 MHz, except the one that specifies ±3 MHz, which was measured using dispersion tuning and side-band modulation, as described in section III.B.

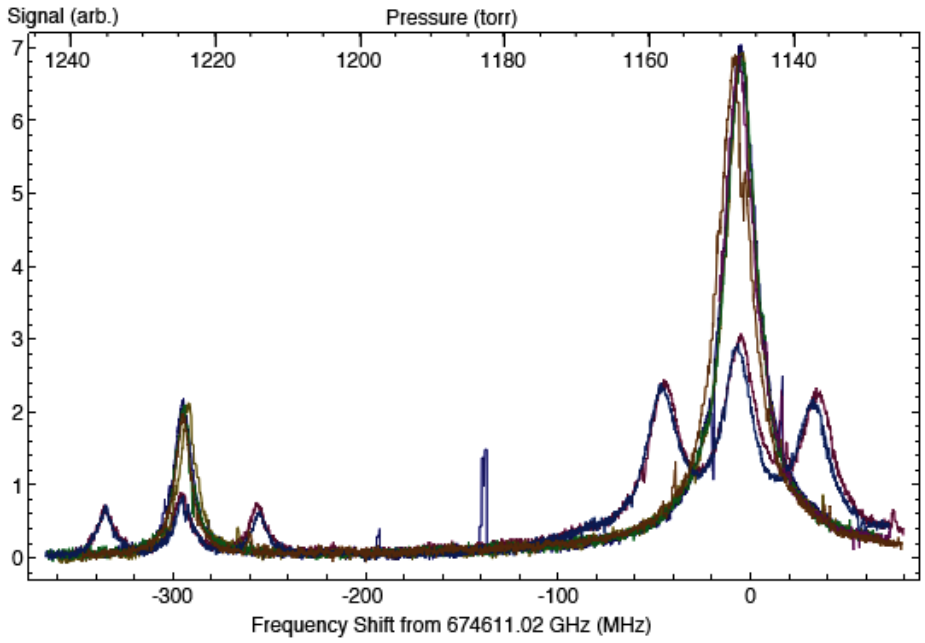


Figure 3.4: Seven CDT scans of two lines, taken over a period of two days. Some data sets include 40.00000 MHz sidebands. The x-axis of this scan comes directly from Eq. 3.8.

peaks have Lorentzian shape, consistent with Doppler-free spectroscopy.

Each individual CDT scan took about two hours to complete. During this time, the feedback output to the PZT voltage for the grating was monitored. This signal, from a typical scan, is shown in Fig. 3.5. The nonlinearity shows the limitation of using a grating scan to obtain a line profile from a signal that may require hours or days to accumulate.

In addition to the CDT scans, we tested temperature dependence of $\Delta f$. This was done by locking the system on the side of line 1525, then heating and cooling the etalon in a closed volume so that $P/T$ was constant, over a few hours while monitoring the signal intensity. We found the dependence to be 20 MHz/$^o$ C, so appropriate

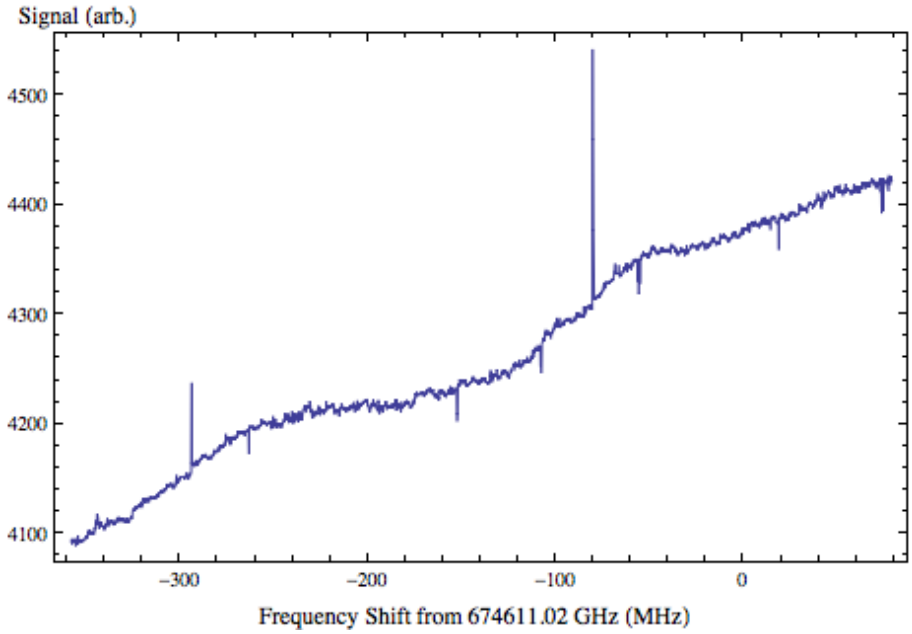


Figure 3.5: The diode grating position at each point during a typical CDT scan. At this scale one can see that a grating scan is quite nonlinear in frequency.

regulation of temperature in the etalon is required.

To measure frequency drift of the blue laser we defined the center from the Lorentzian fit of line 1525 from one data set to be 0 Hz, and then determined the fits' centers of all other data sets relative to it. In doing this over data sets that spanned a 48 hour time period, we found a drift $< 2$ MHz. In calculating $\sigma^2 = \frac{1}{2}\left\langle \left(\frac{\delta f}{f_0}\right)^2 \right\rangle$ from this data, we have a value of $1.3 \times 10^{-18}$. This $\sigma^2$ as a function of time approaches the Allan variance [54].

Originally we attempted to use Carbon Dioxide ($CO_2$) gas for dispersion scanning, which would have allowed for a larger frequency scanning range [55], but found that the temperature stability required for $CO_2$ was beyond our reach. We estimate the temperature dependence of $\Delta f$, using data from Ref. [56] applied to Eq. 3.8, to be nearly 1 GHz/$^o$ C.

### 3.2.4 Concluding Remarks

We find that CDT spectroscopy allows laser locking at any frequency, with a drift less than 2 MHz over days, and a scanning range of nearly 500 MHz. We report 11 intervals in $Te_2$ lines near 444.4 nm with 50 MHz uncertainty with a grating scan, and we demonstrate CDT spectroscopy in reporting one interval with 3 MHz uncertainty. The uncertainty in our measurements is consistent with the $\sim 1$ torr uncertainty of the pressure gauge used (MKS 122BA-10000BB).

This technique may prove useful for studies where short, precise scans or locking to an arbitrary optical frequency are desired such as studies of line profiles, optical

polarization experiments, or studies of molecular species with low data collection rates.

## 3.3 Further Improvements to the Laser System

We now had a working laser setup that could be locked anywhere within a few nanometers of 440 nm, and with pressure adjustments could scan about half a GHz in either direction from the lock point. There were various problems with the system though that made it difficult to work with or in some cases, still not precise enough.

Getting the two lasers locked simultaneously to the cavity was never easy. Once the laser was tuned within a GHz or so of where it needed to be, pressure tuning was needed to simultaneously lock the two. The pressure needed to be adjusted slowly so that the HeNe lock could follow, at a rate of about 100 MHz per hour. Then from there the lock wasn't very stable as the laser frequency was very sensitive to pressure, changing at a rate of 3 MHz per Torr.

Scanning was also very slow. Our pressure gauge was accurate to about 1 Torr, which lead to about a 3 MHz uncertainty of the laser frequency at any position. The price for more precise pressure gauges was steep enough to motivate us to think of other options.

We decided instead to purchase a fiber EOM that worked in the region of 880 nm and make use of the IR port of our laser. The fiber EOM (brand and model) could easily scan over 20 GHz and was as precise as the electronics that drove it. We evacuated the FPI100 and changed the mirrors to suit the 880 nm beam. To make the cavity-to-HeNe lock more stable, we converted the HeNe lock to a Pound-Drever-Hall

(PDH) lock [57] and a temperature control. The temperature control would adjust the temperature of the aluminum cavity body, thereby changing its length, in order to ensure that the PZT voltage locking the cavity didn't drift too far from zero. Finally, we put the cavity and all surrounding optics inside an acoustically isolated, temperature stabilized box, and fiber-coupled all laser beams into the box.

The laser grating control was already capable of scanning over 30 GHz in the IR, 60 GHz in the blue, without a mode hop, but as noted before, the grating voltage to laser frequency relationship is not linear enough to give the desired precision and accuracy. Previously we used cavity "markers" (FPI resonances every FSR or 1 GHz) and corrected for nonlinearity by interpolating between these reference points. However, the nonlinearity was still too great and we continued with dispersion tuning at the time. Now with our new fiber EOM and other existing EOMs, we put 200 MHz and 25 MHz sidebands on the IR beam and ported it into the FPI. We now had a marker every 25 MHz, all across every scan. To optimize marker intensities, we electronically phase locked the EOMs as well. We also purchased a GPS disciplined oscillator and used it to synthesize all of our frequencies more accurately.

These changes resulted in considerable improvements in stability and tunability. We were now able to scan 30 to 35 GHz in the IR, 60 to 70 GHz in the blue, at a time, and measurement of transitions was repeatable to $< 1$ MHz. By linking hundreds of scans together side by side, we scanned several THz worth of tellurium data. We then used a cesium cell to get an absolute frequency reference and record over 9000 tellurium transitions to unprecedented precision. That work is the subject of our next

paper, submitted to the *Journal of the Optical Society of America B* and currently under peer review. Here is that paper, giving the details of these improvements.

## 3.4 Precise, Tunable frequency source, and the measurement of 9000 $^{130}Te_2$ transitions from 443.2 to 451.4 nm

### 3.4.1 Introduction

Tunable, frequency-stabilized lasers are necessary for a wide variety of experiments, such as searches for the electron's electric dipole moment [58], laser cooling experiments [59], precision spectroscopy [60], ion trapping [61], and studies of few-body physics [62] to name a few. Frequency modulation spectroscopy [63], dispersion tuning spectroscopy [46] and related methods have achieved precisions around 1 in $10^9$ $\Delta$Hz/Hz, but they have limited scanning ranges of at most a few GHz. Frequency combs [64, 65] are more precise and capable of covering much larger ranges, but as of this printing are quite costly. Alternative methods are desired for many labs that need to conduct high-precision experiments without an onerous capital equipment burden. The augmented laser system we present here is capable of staying locked with a drift under $1{:}10^{10}$ for months, scanning $> 10$ THz with optical adjustments, and can reliably return to any frequency in its range with a sub-MHz uncertainty. We've used this system to catalog over 9000 $^{130}Te_2$ transitions. Many of these transitions were measured previously [13], but Doppler broadening buried many of the transitions and uncertainties were around 100 MHz [66].

### 3.4.2 Setup - frequency source

For our measurements we use a Topic SHG Pro laser system. This system has a primary oscillator laser diode near 890 nm (IR) which is frequency-doubled internally using a bowtie cavity. The resulting blue light is sent to the $Te_2$ cell described in Sec. 3.4.3. A fraction of the IR is ported out of the laser. The IR is then split and sent to both the wave meter (Burleigh WA-1000) and the Fabry-Pérot cavity (Toptica FPI-100), as seen in Fig. 3.6.

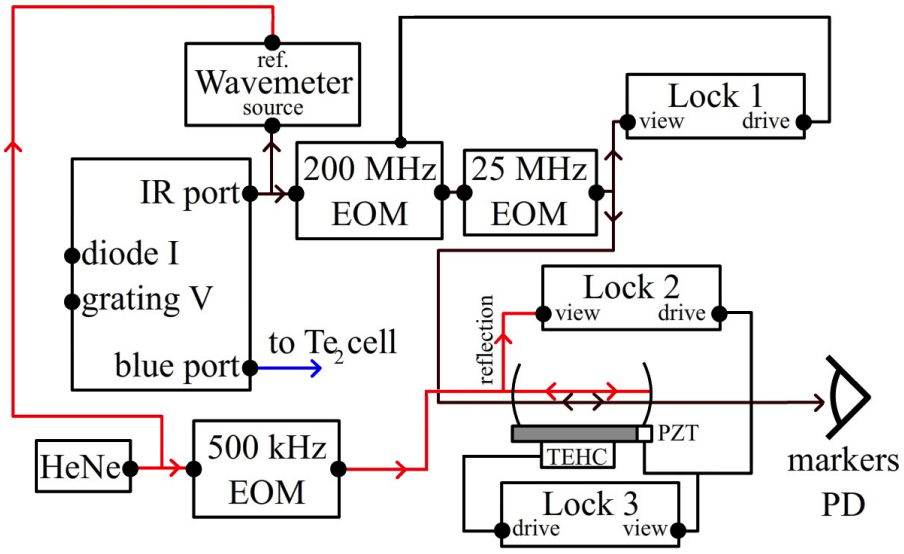


Figure 3.6: Setup of the laser and Fabry-Pérot cavity.

In the diagram, lock schematics have been simplified into flow charts. Lock 1 is a standard servo lock to lock the phase on the electro-optical phase modulator (EOM), Lock 2 is a Pound-Drever-Hall (PDH) setup to lock the FPI to the HeNe laser [57], and Lock 3 is a servo lock done in LabView to hold the voltage on the piezoelectric transducer (PZT) to zero. The 200 MHz and 25 MHz sources are synthesized from a

10 MHz GPS disciplined oscillator, holding drifts under $1 \times 10^{-10} \Delta f/f$. The following subsections describe the active and passive stabilization mechanisms used on the cavity and the surrounding laser setup.

### The optical cavity

The optical resonator used was an evacuated Fabry-Pérot cavity with a finesse around 700 and a free spectral range (FSR) of around 2 GHz. The FSR is discussed in detail in section 4, and the stabilization of the cavity is described here.

The cavity and all surrounding optics are inside of a heavy, two layer box. Electronic cables and gas tubes come in through the bottom layer where they are held in 100 lbs of lead shot, then ported through to the top layer where they make their connections. This is to establish acoustical isolation. The entire box is also mounted on a floated table.

The cavity is actively held resonant to a stabilized HeNe laser (mirco-G) by means of a PDH lock (Lock 2). One of the mirrors is adjusted by a PZT in this lock, but over long time periods the average voltage on the PZT drifts out of the low voltage servo-lock range. For this reason we've installed a second, slower feedback (Lock 3) to the temperature of the aluminum body by means of a thermoelectric heating and cooling device (TEHC), working in response to the demodulated voltage on the PZT and keeping it at zero. With this setup the cavity stays locked for months, and the transmitted line width matches that of the HeNe laser, which is around 200 kHz. This value is discussed further in Sec. 3.4.5, including an Allan deviation measurement.

### The laser

The frequency for an experiment is scanned by turning the grating, by adjusting the voltage on the PZT attached to it. The voltage to laser frequency relationship is nonlinear, so during scans the IR from the laser is mode-matched to the $\mathrm{TEM}_{0,0,n}$ mode of the confocal cavity (FPI100). Transmission resonances are detected every FSR, giving us frequency markers about every 2 GHz (referred to as "markers" from here on). To achieve the level of precision we needed for this measurement, many more markers were necessary to give a sufficiently precise interpolation. Thus, the beam was aligned slightly off-center, giving smaller resonances every half FSR. Sidebands were introduced on the IR by two electro-optical modulators (EOM), one set to 200 MHz and the other to 25 MHz. With this setup, we had a cavity resonance every 25 MHz all the way across a scan (see Fig. 3.7), and the interpolation was so reliable that repeated measurements of the same line never differed by more than 200 kHz.

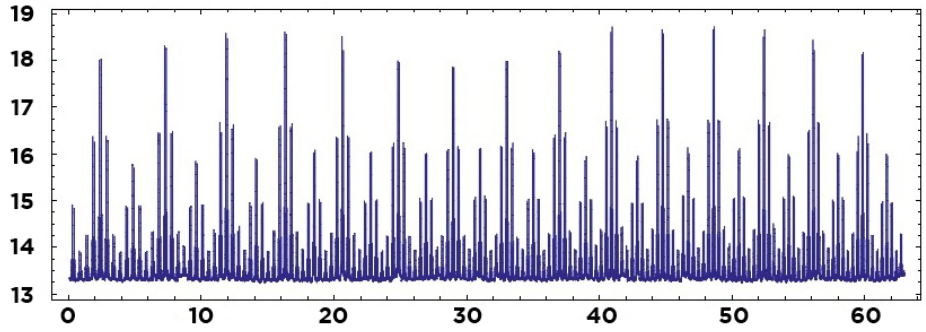


Figure 3.7: IR resonances in the cavity used as markers for interpolation (arb). Sidebands are created by the EOMs, and a smaller set of markers appears halfway between each larger set because of the misalignment.

The transmission of the 200 MHz EOM needed to be stabilized by adjusting the DC bias to enhance the relative sideband intensity. The relative sideband intensities are a maximum when total transmission is a minimum. We locked to this configuration using a servo lock (Lock 3).

For diagnostic purposes, RF sideband scanning [67] with this setup may be desired. To accomplish this, a sideband generated by the waveguide EOM can be locked to the FPI100, and the frequency of the waveguide EOM can be swept to force the central laser frequency to scan. We did this by removing the 25 MHz EOM and connecting the "drive" of Lock 1 to the laser's IR diode instead of the waveguide EOM's frequency control. As discussed in section 3.4.5, we employed this technique for calibration and Alan deviation measurements.

**Repeatability**

The wavemeter used was a Burleigh WA-1000 with enhanced stability and accuracy due to the stabilized HeNe reference, precise to $\sim 100$ MHz. If a particular frequency was desired, the wavemeter was precise enough to unambiguously determine the appropriate FSR marker as we adjusted the laser. From there, a sideband generated by the waveguide EOM can be tuned to a cavity resonance and used, via a PDH lock, to stabilize the laser to an arbitrary frequency that replicates the HeNe laser's stability, $< 200$ kHz.

This method depends heavily on the long-term stabilization of the cavity-to-HeNe lock, which is why we used the TEHC and held the PZT voltage fixed by adjusting the

aluminum body temperature with LabView. Should anything else go wrong though, there was a second failsafe. By unlocking the cavity and moving the temperature we could re-lock on another resonance. This slightly changes the FSR of the cavity and shifts the positions of our cavity markers. Therefore, we needed to know without doubt that we were on the same resonance when we had to re-lock. Using a spectral line or series of lines from $^{130}Te_2$, or using cesium D1 transitions [68], we measured the separation between the transition and the nearest cavity marker. This number changes in a well defined way depending on the HeNe resonance to which the cavity was locked. We could thus unambiguously relock the cavity to the correct HeNe resonance. Later we used this method to our advantage in another way, where we used this dependence of FSR on HeNe longitudinal mode number to measure the FSR more carefully, as explained in Sec. 3.4.4.

### 3.4.3 Setup - $Te_2$ cell

We took saturated-absorption spectra of $^{130}Te_2$ by means of counter-propagating beams and a lock-in amplifier (see Fig. 3.8). The initial blue beam is split through a polarizing beam splitter (PBS), creating a "pump" beam (transmitted) and a "probe" beam (reflected). The pump beam passes through wave plates, an EOM, and another PBS, which together act as a chopper, blocking and unblocking the beam, when an oscillating voltage is applied to the EOM (we used 30 kHz). The probe beam is not chopped. When there is a tellurium transition the chopping is effectively written onto the probe beam and detected by the lock-in amplifier, referenced to the same 30 kHz.

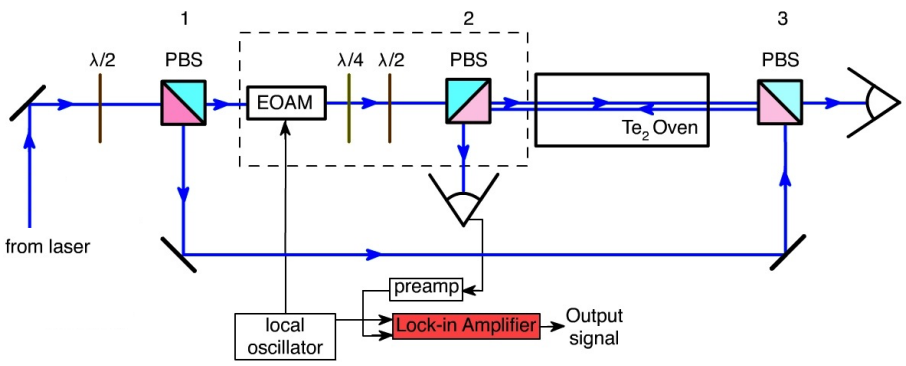


Figure 3.8: Our setup used for saturated-absorption spectroscopy of $^{130}Te_2$.

The transmitted pump beam is also detected and recorded. The laser power is stabilized by feedback from the IR measured intensity to an internal tapered amplifier current through a servo (not pictured).

### 3.4.4 Free-spectral range of the cavity

The availability of markers separated by only 25 MHz and spanning from one FSR marker to the next was invaluable for us and yielded very precise and reliable interpolations for determining the frequency-axis of our data. It does not, however, contribute to the long-distance precision of our data. When scanning over hundreds of GHz (or hundreds of FSRs), it is our knowledge of the free-spectral range of the cavity that is important. For this reason, careful determination of its value was needed. We measured the FSR with two independent methods.

### Wavemeter measurement of the free-spectral-range

The first method was the most direct approach: simply measure the distance between tens of thousands of markers. The IR diode was capable of scanning over 200 nm, no longer limited by the specs of the doubling cavity. With a little averaging, we obtained about a 100 MHz precision on the wavemeter, and by successively making bigger and bigger jumps it only took a few days to measure the distance across about 13000 FSRs, at which point we were limited by dispersion correction of air in the wavemeter.

### Cavity re-lock and the Cs cell, used to measure the free-spectral-range

As mentioned in Sec. 3.4.2, if we broke the cavity-to-HeNe lock and adjusted the temperature, we could lock to another HeNe resonance, at a different cavity length [69]. Here we made use of a cesium cell and cesium's well-documented D1 transitions in the region [68], measured to a precision of tens of kHz. For this experiment, the waveguide EOM was used to create sidebands of the IR beam which was locked to the cavity, while the cavity was locked to the HeNe, and then by sweeping the EOM frequency we scanned the central IR frequency across the nearest Cs D1 transition. This way we could accurately determine how far the Cs transition was from the nearest cavity marker, and we could repeat this process for different cavity locks. At a particular Cs measurement, it can be said that:

$$(N+n)\nu_{FSR}(n) + \Delta_n^a = \nu_{Cs}^a \tag{3.9}$$

where $N$ is the (large) number of IR half-wavelengths in the cavity at some reference point, $n$ is the (small) number of IR half-wavelengths past that, $\nu_{FSR}(n)$ is the free-spectral range of the cavity for HeNe resonance $n$, $\Delta_n^a$ is the measured frequency distance from the nearest marker, and $\nu_{Cs}^a$ is the frequency of the cesium transition, known to a few kHz [68]. In the equation $a$ is from 1 to 4, as there are four Cs transitions being used here from Ref. [68]. At any particular HeNe resonance $n$, four values of $\Delta_n$ can be measured with $\sim 50$ kHz uncertainty, and the value of $\nu_{FSR}$ for that $n$ can be estimated to about 25 kHz uncertainty. The free spectral range is defined to be $\nu_{FSR} = \frac{c}{2L}$ with $L$ as the cavity length. If we change $L$ by moving to an adjacent HeNe resonance, then $L \to L + \lambda_{HeNe}/2$, and the FSR shifts slightly:

$$\frac{c}{2L} \to \frac{c}{2\left(L + \frac{\lambda_{HeNe}}{2}\right)} \approx \frac{c}{2L}\left(1 - n\frac{\lambda_{HeNe}}{2L}\right) \tag{3.10}$$

Even for $n \sim 100$, $n\lambda/2L \sim 10^{-4}$ so the approximation remains valid. $\lambda_{HeNe}$ was known to over 8 digits as measured by the manufacturer, and from there we made measurements of $\nu_{FSR}$ for many different values of $n$, and used that information to find $N$ and $\nu_{FSR}(0)$. We were able to do this for about 100 different $n$, and found the two quantities to about six digits, or a precision of $< 15$ kHz for the FSR. It is worth mentioning here that $N$ is in fact *not* an integer, as the Gouy phase, offset, and non-zero skin-depth of the mirrors add some fractional part $\delta_N$.

This method was limited by our lack of knowledge of $\delta_N$ for our setup, and by the fact that $n$ is limited to the confocal region [70] for our mirrors. The final uncertainties obtained are discussed next.

### 3.4.5 Uncertainty considerations

Three distinct types of uncertainty are relevant here: short-range, long-range, and absolute.

The short range uncertainty is the uncertainty between measurements of a few tens of FSR's apart or less (approx 0-100 GHz). This is most easily determined empirically; from rescanning certain regions multiple times and seeing how well the measurements agree. Theoretically, this uncertainty comes from the interpolation of the 25 MHz markers, which are limited by the transmitted bandwidth of the cavity, which is in turn limited by the instability of the HeNe laser. The HeNe laser documentation says its short-term stability is $< 200$ kHz, so we expect something in that neighborhood, and indeed, when re-measuring transition energy differences we consistently found agreement to better than 200 kHz.

The long-range stability depends entirely on our knowledge of the FSR. When adjacent data sets are linked together in the processing of data, we did so by counting markers and matching them, so there is no significant error in the linking of data sets together in itself. If on the other hand, we were mistaken about the FSR by 100 kHz, then after 1000 FSRs the uncertainty would add (*not* in quadrature) to 100 MHz. Our two measurements measured in section 4 each had uncertainties of 15 kHz, so the weighted average measurement uncertainty was 10 kHz. This would mean that the frequency difference measured for two transitions that are 2000 GHz apart would be 10 MHz.

The absolute frequency measurement relies on an external frequency reference. The ground state hyperfine splitting of cesium used to define the second contains four transitions in the IR [68] that, if doubled, would be in the range of the tellurium transitions. For this reason we used the IR port of our laser to measure the four transitions and get an absolute frequency measurement of the adjacent cavity markers (used in processing tellurium data). For this measurement the cavity was locked to the HeNe, and a sideband of the IR was locked to the cavity. The RF frequency making the sideband via the EOM was scanned, keeping the sideband locked while the central IR frequency shifted, as described in the *The laser* section above, and similarly in Ref. [67]. This precisely scanned RF frequency was then used to measure the saturated absorption of cesium. We now had an absolute frequency reference precise to about $\sim 50$ kHz, or about $10^{-11}\Delta f/f$.

This same setup provided a good opportunity to carefully characterize the cavity's long term stability as well. We measured a transition back and forth, tens of thousands of times, for 3 weeks, and used this information to get the Allan deviation of the cavity-to-HeNe lock. This measurement is shown in Fig. 3.9. We found our measured Allan deviation to be consistent with that of the HeNe laser according to its documentation.

The absolute frequency uncertainty therefore linearly increases with frequency-distance from double the first measured cesium transition:

$$2f_{D1}^{F_g=4\rightarrow F_e=3} = 2 \times 335111370.21(5) \text{ MHz}.$$

This point is also nearly the center point for our tellurium data. Our measurements span about $\pm 6$ THz from the center, yielding a 30 MHz uncertainty at the extreme

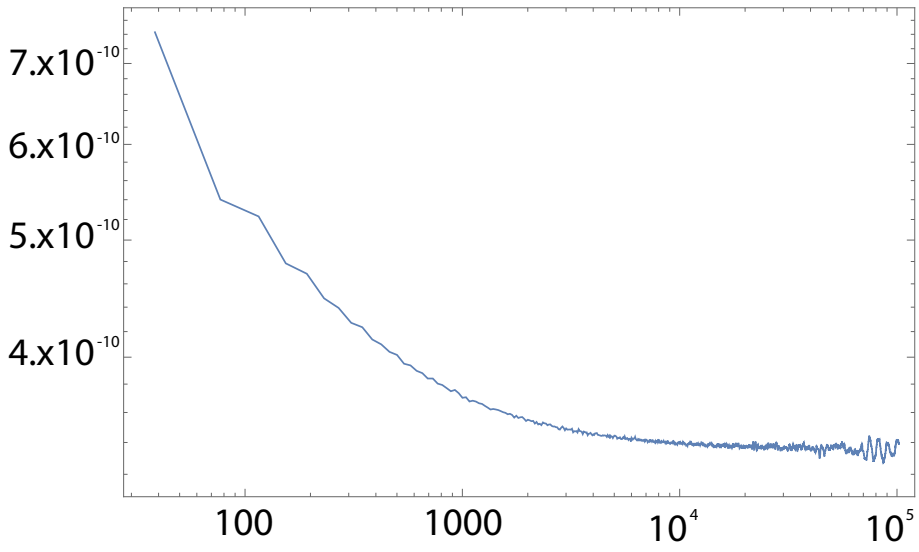


Figure 3.9: Allan deviation for Cs line center measurements ($\Delta f/f$ vs. sec.)

edges, and an overall average uncertainty of 15 MHz. There is an additional systematic error to consider here: we did not use a cold finger in the tellurium cell and the vapor pressure shift from our cell would add an estimated 6 MHz uncertainty everywhere [16], which brings the total absolute uncertainty average to 16 MHz, or about $2 \times 10^{-8} \Delta f/f$. It's worth noting that in the region from 669900 to 670500 GHz the absolute frequency uncertainty is comparable to the short-range uncertainty, staying under $1 \times 10^{-9} \Delta f/f$. As one gets closer to the center, the uncertainty hits the floor (from short-range) of 200 kHz.

### 3.4.6 Conclusion

With disciplined oscillators, a long-term highly stable optical cavity, and frequency resonances every 25 MHz recorded as the laser sweeps and used for interpolation, we've achieved a precise scanning method that can be tuned over tens of THz in the

blue part of the visible spectrum. With such a stable, long lasting cavity lock, the laser can also be locked at any particular frequency in this region for months at a time, drifting less than $1 \times 10^{-10} \Delta f/f$. After characterizing this system and making absolute frequency reference measurements of Cs, we've used it to scan over 12 THz of $^{130}Te_2$ data, cataloging over 9000 transitions. This data may prove useful as a catalogue of frequency references, or for spectroscopic studies of heavy molecules [18]. We'd like to thank Chris McRaven and Neil Shafer-Ray for thoughtful contributions, and the National Science Foundation and the University of Oklahoma Research Council for support.

# Chapter 4

# Improved analytic potentials and spectroscopic properties of $^{130}Te_2$

## 4.1 Introduction

Diatomic tellurium is widely used as a frequency reference for optical experiments [13, 16, 66, 71]. These works rarely discuss spectroscopic properties of tellurium though as their interest is primarily in documenting optical frequencies used as standards for other experiments. Because of it's relatively small rotation and vibration constants [72], $^{130}Te_2$'s transitions are more closely spaced than most diatomic molecules. With a line density of around 1 transition every GHz, spectroscopic assignments can be very tedious and difficult. A sample of our data is depicted in Fig. 4.1, demonstrating this extreme line density.

This high line density is largely due to the fact that its vibrational bands have considerable overlap with many neighboring vibrational bands in the displayed optical spectrum. An approximate simulation over about 60% of the region depicted in Fig. 4.1, showing only half[1] of the X0←B0 transitions up to vibrational level $v = 8$ and rotational level $J = 150$ is depicted in Fig. 4.2.

For these reasons, spectroscopic study of $^{130}Te_2$ has not progressed since 1982 [73]. Although many newer papers with $^{130}Te_2$ exist, the lines remain unassigned, and are referred to by arbitrary numbers given by Cariou in 1980 [13]. The ground state

[1] In the next section is a basic treatment of diatomic spectra, where rotational $P$ and $R$ branches will be introduced. Fig. 4.2 only includes the $R$ branches, thus "half" the transitions.

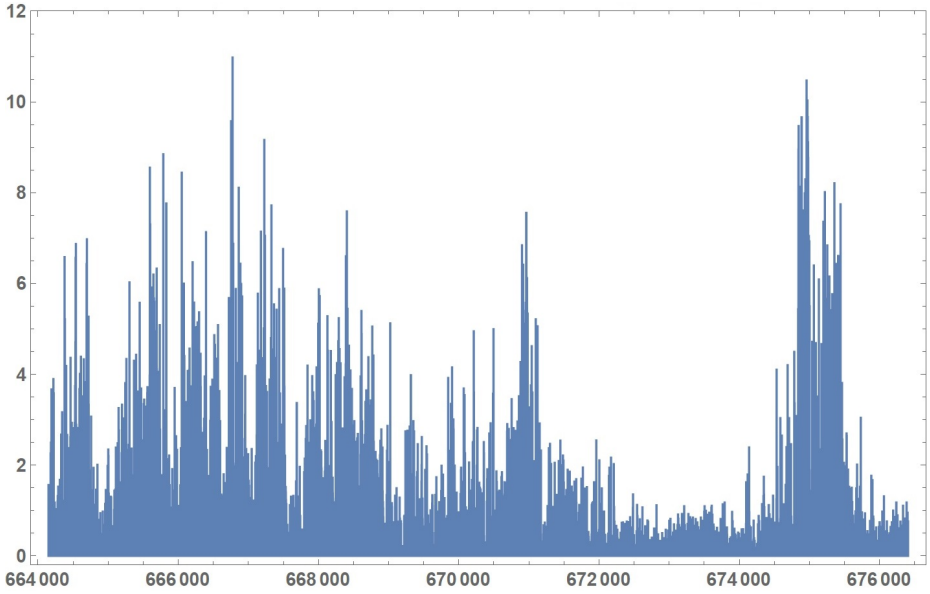


Figure 4.1: $^{130}Te_2$ transitions between 664 and 676 THz (arb. vs. GHz)

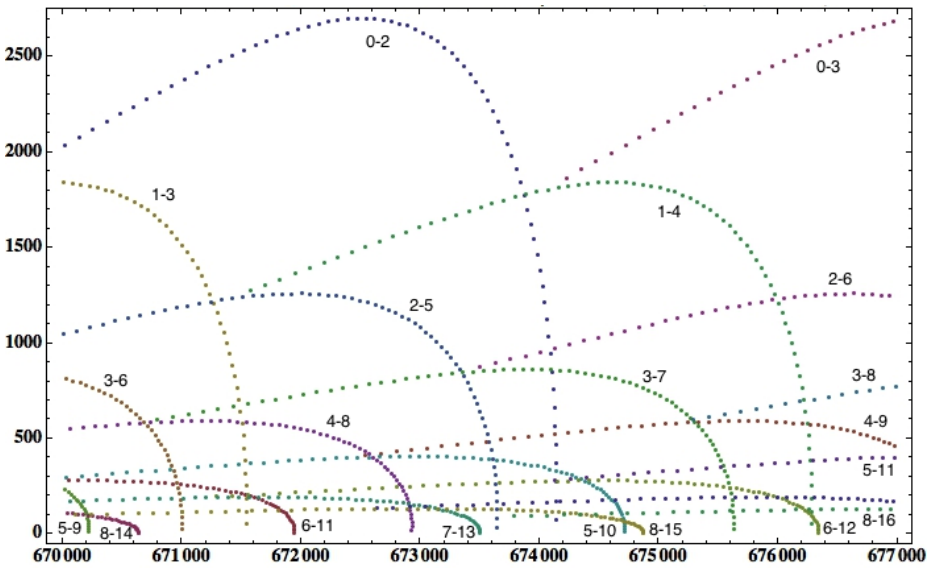


Figure 4.2: R branch transitions of $^{130}Te_2$ between 670 and 677 THz (arb. vs. GHz). The vertical axis represents weighting according to Maxwell-Boltzmann populations and rotational degeneracy factors.

was decently characterized using Fourier Transform Spectrometry on Laser Induced Fluorescence spectra of $^{130}Te_2$ in 1982 [73], but excited-state information remained in bits and pieces. Further, the studies utilized Dunham's model [19], and since then, more accurate potentials have been developed [18]. At this point I will discuss these diatomic potentials further.

## 4.2 The Dunham model for diatomic molecules

Traditionally, diatomic molecules are characterized by Dunham's model [19]. I will give a brief overview of this model now. Diatomic molecules have electronic energy structure similar to that of atoms, but they possess two additional degrees of freedom: vibration and rotation of the nuclei with respect to each other. The vibration of two nuclei with respect to each other can be modeled as a quantum harmonic oscillator and this yields energy levels of the form: $E_v = \hbar\omega(v + 1/2)$ where $v$ is the vibrational quantum number. Similarly, the rotation of two nuclei about each other are modeled with the quantum angular momentum operator and yield energy levels of the form: $E_J = \frac{\hbar^2}{2I}J(J+1)$ where $J$ is the rotational quantum number and $I$ is the moment of inertia. Each of these simple models works without the other. Dunham's model addresses what happens when rotation and vibration occur at the same time, a system often called a *non-rigid rotor*. This model is the same to zeroth order, but higher orders introduce coupling terms, so that we have:

$$E_{v,J} = \sum_{i,k} Y_{i,k} \left(v + \frac{1}{2}\right)^i J^k (J+1)^k \tag{4.1}$$

for the energy of a non-rigid rotor with vibrational and rotational quantum numbers $v$ and $J$ respectively. These ${Y_{i,k}}^2$ coefficients can be connected to the historically familiar band spectrum constants:

$$\begin{aligned} Y_{10} &\sim \omega_e \quad Y_{20} \sim -\omega_e x \quad Y_{30} \sim \omega_e y \\ Y_{01} &\sim B_e \quad Y_{11} \sim -\alpha_e \quad Y_{21} \sim \gamma_e \\ Y_{02} &\sim D_e \quad Y_{12} \sim \beta_e \quad Y_{40} \sim \omega_e z \end{aligned} \tag{4.2}$$

Each of these $Y_{i,k}$ coefficients differs from its corresponding spectroscopic constant by order $B_e^2/\omega_e^2$ or higher [19]. The quantity $B_e^2/\omega_e^2$ is very small for most diatomic molecules; for $^{130}Te_2$ and NO ground states it is approximately $2.5\times10^{-8}$ and $7.7\times10^{-7}$, respectively. As $B_e$ corresponds to the separation between rotational levels and $\omega_e$ corresponds to the separation between vibrational levels, this means that neighboring vibrational levels are much more separated than neighboring rotational levels, as seen in Fig. 4.2. For this reason, the equations describing diatomic energy levels are typically shown including a polynomial in $J(J+1)$, followed by the polynomials of how the $J(J+1)$ polynomial coefficients evolve with $v$. The energy levels for $^{130}Te_2$

[2]These $Y_{i,k}$ are not to be confused with the spherical harmonics $Y_m^l$

described under Dunham's model are therefore[3]:

$$E_{v,J} = T_e + G_v + B_v J(J+1) - D_v J^2(J+1)^2 + H_v J^3(J+1)^3 + ... \quad (4.3)$$

$$G_v = \omega_e(v+\frac{1}{2}) - \omega_e x_e(v+\frac{1}{2})^2 + \omega_e y_e(v+\frac{1}{2})^3 + \omega_e z_{e1}(v+\frac{1}{2})^4 + ... \quad (4.4)$$

$$B_v = B_e - \alpha_e(v+\frac{1}{2}) + \gamma_{e1}(v+\frac{1}{2})^2 + ... \quad (4.5)$$

$$D_v = D_e + \beta_{e1}(v+\frac{1}{2}) + \beta_{e2}(v+\frac{1}{2})^2 + ... \quad (4.6)$$

$$H_v = H_e + g_1(v+\frac{1}{2}) + g_2(v+\frac{1}{2})^2 + ... \quad (4.7)$$

Here, Eq. 4.3 gives the energy for a $^{130}Te_2$ molecule with vibrational and rotational quantum numbers $v$ and $J$, respectively. $T_e$ is a constant that represents the bottom of the potential curve for the given electronic state. For the ground electronic state X0($^3\Sigma_g^-$), $T_e$ is defined to be zero. All the other constants are the Dunham parameters. For reference, $B_v$ is referred to as the rotational constant, $D_v$ and $H_v$ the centrifugal distortion constants, $\omega_e$ the harmonic frequency constant, and its corrections ($\omega_e x_e$, $\omega_e y_e$, etc.) are called the anharmonicity constants. The potentials for the X0 and B0 states are plotted vs. internuclear distance in Fig. 4.3.

Although we ultimately would use the Morse Long-Range (MLR) potential from Ref. [18] to characterize $^{130}Te_2$, fitting that potential requires a few hundred line assignments first. Using references [73] and [72] we were able to fill in rough values for the Dunham constants for the X0 and B0 states, and make careful adjustments from there to get better values as we assigned the lines. I was able to assign 1400 transitions to spectroscopic states. In doing so, I improved the precision for Dunham's

[3]The tellurium transitions we study here are all from the X0 state to the B0 state, and both of those states are $^3\Sigma^-$. This means they are both always $f$-states so no $e/f$ parity term is needed as in Eq. 2.5.

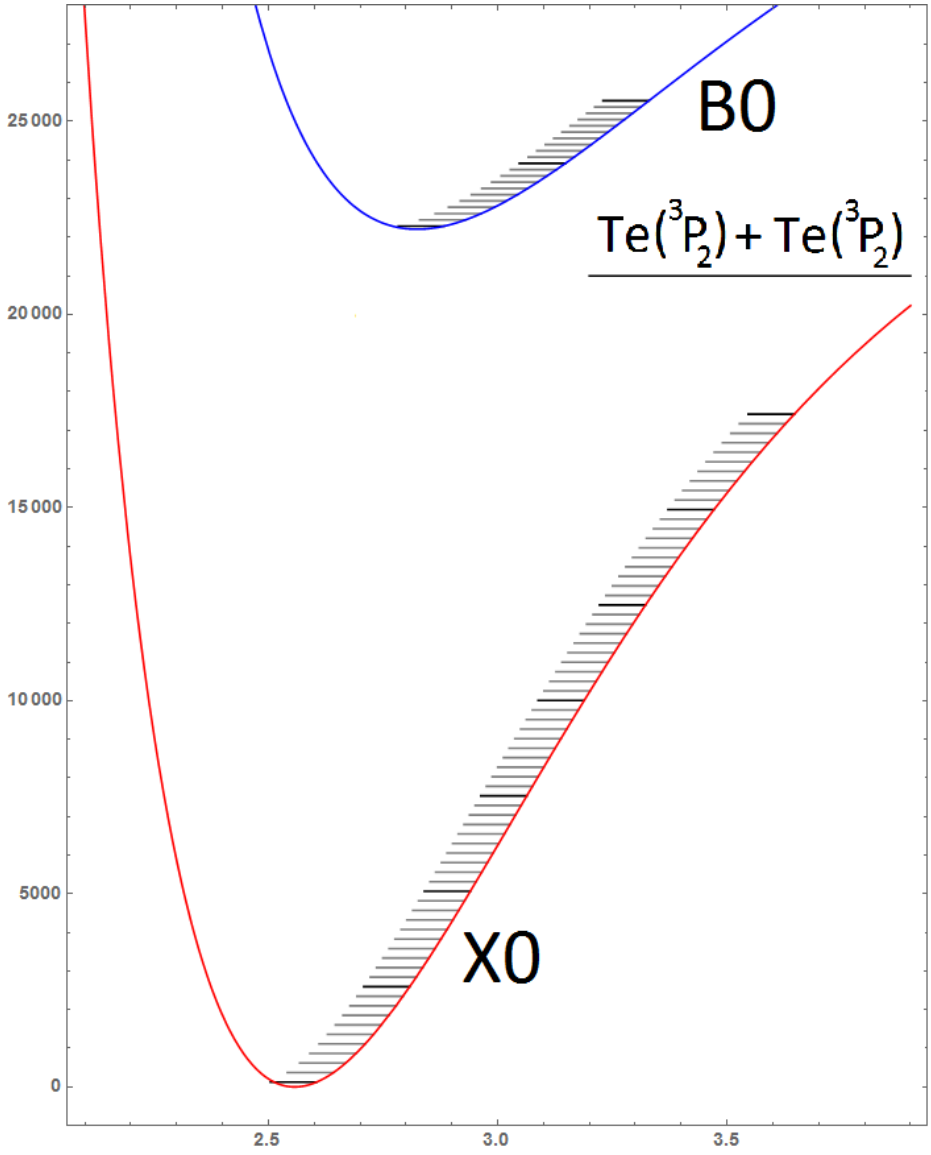


Figure 4.3: Potentials for $^{130}Te_2$ X0 and B0 states with internuclear distance ($cm^{-1}$ vs Å). The energy of dissociation for the ground state is shown in black. The vibrational levels are shown in gray, with $v = 0, 10, ...$ in black.

constants by one to three orders of magnitude. Those were further improved later after utilizing the MLR potential, thus they are given in a later section. I now turn our attention to the MLR potential.

## 4.3 The Morse-Long-Range potential for diatomic molecules

The diatomic model based on Dunham's polynomial expansion is helpful for making spectroscopic assignments in small regions, but it has been notorious for not matching up upon extrapolation [18]. The MLR potential is designed to imitate the actual shape of the potential curve instead of forcing a polynomial fit. The MLR model for radial potential energy functions is:

$$V_{\mathrm{MLR}} = \mathcal{D}_e \left(1 - \frac{u_{\mathrm{LR}}(r)}{u_{\mathrm{LR}}(r_e)} e^{-\beta(r)\cdot y_p^{eq}(r)}\right)^2. \tag{4.8}$$

Here, $\mathcal{D}_e$ is the dissociation limit and the radial variable $y$, defined as:

$$y_p^{eq}(r) \equiv \frac{r^p - r_{eq}^p}{r^p + r_{eq}^p} \tag{4.9}$$

is used, where $r_{eq}$ is the euqilibrium internuclear distance. The function $\beta(r)$ in the exponential is commonly written as the polynomial:

$$\beta(r) \equiv y_p^{eq}(r)\beta_\infty + (1 - y_p^{eq}(r)) \sum_{i=0}^{N} \beta_i y_q^{eq}(r)^i \tag{4.10}$$

with $\beta_\infty$ defined as $\lim_{r\to\infty} \beta(r) = \ln(2\mathcal{D}_e/u_{\mathrm{LR}}(r_e))$. The function $u_{\mathrm{LR}}(r)$ in Eq. 4.8 is defined by the dispersion coefficients particular to the molecule [74, 75]:

$$u_{\mathrm{LR}}(r) = \sum_{i=1} D_{m_i} \frac{C_{m_i}}{r^{m_i}} \tag{4.11}$$

with the damping function as described in Refs. [21, 76, 77]:

$$D_{m_i}(r) = \left(1 - e^{-\left(\frac{3.30\rho_{ab}r}{m_i} + \frac{0.423\rho_{ab}^2 r^2}{m_i}\right)}\right)^{m_i - 1}. \tag{4.12}$$

The damping function has the single parameter $\rho_{ab}$. The $\beta_i$'s, $r_{eq}$, and $\mathcal{D}_e$ are the fit parameters for the MLR potential. We found the dispersion coefficients ($C_m$) for $^{130}Te_2$ in Ref. [78]. The powers $p$ and $q$ seen in Eqs. 4.8-4.10 can be chosen for the best fit. According to Ref. [18], it is typically best to set $p = m_{next} - m_1$, the difference between the $m$'s of the first neglected $C_m/r_m$ term and the leading $C_m/r_m$ term, and $q$ can be set to any low integer $\neq p$ without affecting the deviation of the result. The equilibrium internuclear distance $r_{eq}$ is shown in these equations, but any reference distance $r_{ref}$ can be used in its place, in Eqs. 4.9-4.11.

This formulation of the diatomic potential has been successful at characterizing various molecules [18, 20, 21], and there is interest in its application to heavy diatomics (such as tellurium) which are difficult to characterize otherwise. It has the added advantage of having many fewer parameters than the Dunham potential, indicating that the function is more physically meaningful. We now look at the results of applying this formalism to our $^{130}Te_2$ data.

## 4.4 Our reported parameters for $^{130}Te_2$

As mentioned before, we measured over 9000 optical transitions in $^{130}Te_2$, and assigned 1400 to spectroscopic states. These matched transitions are from 13 vibrational bands.

One example of a matched $P, R^4$ set of transitions is shown in Fig. 4.4. Most of these bands span over multiple THz, so only a portion of matched lines are shown.

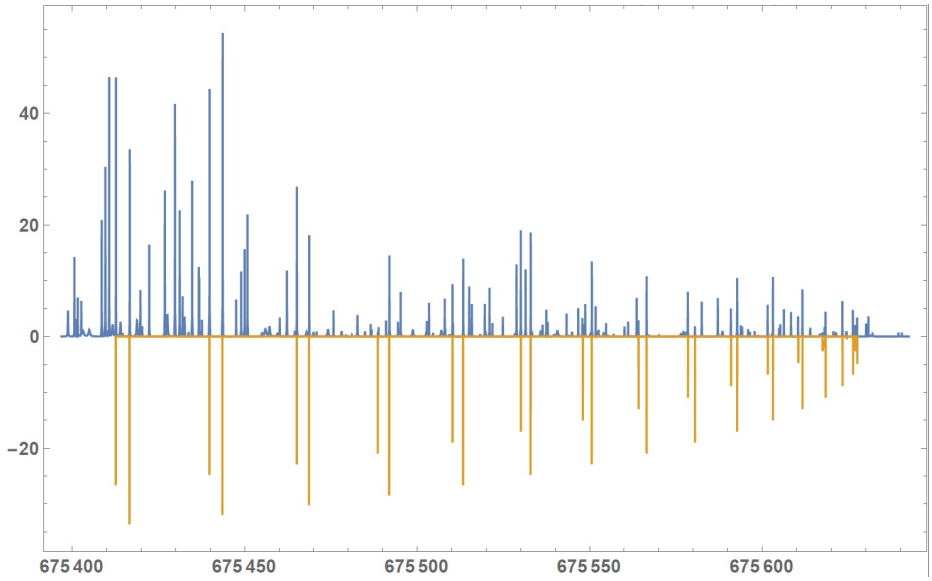


Figure 4.4: Demonstration of several matching $P, R$ pairs from the $v = 7 \leftarrow v' = 3$ band (arb. vs. GHz). The data is shown upright and the simulated transitions are upside-down.

These measurements were made to better than $10^{-8}$ $\Delta f/f$, and from them we expect to yield unprecedented precision for the constants of $^{130}Te_2$. With assistance from Dr. Nikesh Dattani from the University of Singapore and the use of software developed by Dr. Robert Le Roy from the University of Waterloo [79] we characterized $^{130}Te_2$'s ground state and first excited state (X0 and B0), and the results are in Table 4.1.

The results in Table 4.1 are for the ground state X0($^3\Sigma_g^-$). This characterizes the ground state to a higher precision than that of Ref. [73] with about one-third

[4] $P$ and $R$ refer to branches where $\Delta J = -1$ and 1, respectively. The selection rules for this system dictate that if total spin $S$ does not change, then $\Delta J = \pm 1$ [39].

| Parameter | Base Value | Multiplier | Comment |
|---|---|---|---|
| $\rho_{ab}$ | 0.80 | 1 | from the damping function equation |
| $C_6$ | 3.05111 | $10^6$ | from Ref. [78] |
| $C_8$ | 3.29663 | $10^8$ | from Ref. [78] |
| $C_{10}$ | 1.04331 | $10^10$ | from Ref. [78] |
| $\mathcal{D}_e$ | 2.134±0.002 | $10^4$ | dissociation energy for X0 state |
| $r_{eq}$ | 2.5577273±0.0000088 | 1 | equilibrium internuclear distance for X0 state |
| $p$ | 5 | 1 | chosen parameter |
| $q$ | 3 | 1 | chosen parameter |
| $r_{ref}$ | 3.00 | 1 | chosen reference internuclear distance |
| $\beta_0$ | 3.680172074734 | $10^{-1}$ | fit parameters for MLR potential |
| $\beta_1$ | 1.170464231242 | 1 | ⋮ |
| $\beta_2$ | -2.643780300486 | 1 | |
| $\beta_3$ | 6.255288995689 | 10 | |
| $\beta_4$ | 1.168975197973 | $10^3$ | |
| $\beta_5$ | 7.586665466421 | $10^3$ | |
| $\beta_6$ | 2.489537273571 | $10^4$ | |
| $\beta_7$ | 4.156601950189 | $10^4$ | |
| $\beta_8$ | 2.810811598243 | $10^4$ | |

Table 4.1: MLR Parameters for $^{130}Te_2$ X0 state. All lengths are Å, all energies are $cm^{-1}$, and all $\beta_i$ are dimensionless.

the number of parameters. The quality of this fit was determined via deviation root-mean-square to a value of 0.63. This means that each transition's measured value, minus its MLR calculated value, divided by its reported uncertainty, was calculated, and the root mean square was taken for all of them. A value less than one means the fit was good. The value of 0.63 was a little too good; this indicates that we may have overestimated the uncertainty.

As mentioned in Sec. 3.4.5, the uncertainty of our measured transitions grows linearly as the measured frequency gets further from the Cs frequency reference. The actual uncertainties used in this fit, as a function of measured frequency, are plotted in Fig. 4.5.

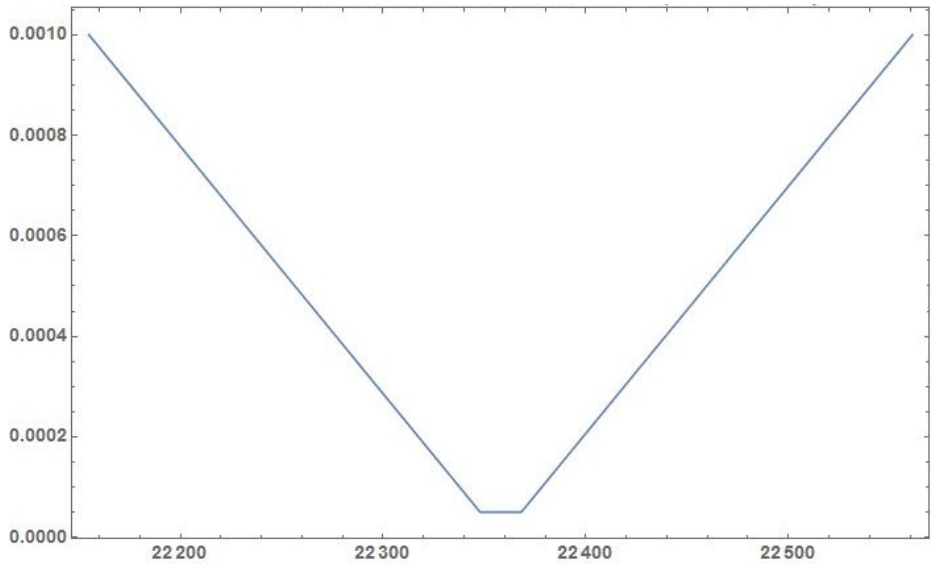


Figure 4.5: Uncertainy of $^{130}Te_2$ measurements and dependence on measured frequency ($cm^{-1}$ vs. $cm^{-1}$)

The total uncertainy's shape comes primarily from the uncertainty in the FSR of the cavity used. Supposing the FSR was 10 kHz too high, then after 1000 FSRs

the frequency axis is 10 MHz too high. This continual shift would add linearly, not in quadrature. If we slightly overestimated our uncertainty in the FSR, the effect would be a decreased slope in Fig. 4.5, or a more flattened 'V'-shape. This appears to be the case, since our DRMS was so low. We cannot justifiably lower the reported uncertainty, but it appears that the FSR used was (perhaps by luck) more accurate than we realized.

We also extracted from this work the MLR fit parameters for the B0 state, and they are shown in Table 4.2.

As I mentioned earlier, we were able to refine the Dunham parameters afterwards. I list them here in Table 4.3. These Dunham parameters give the same function and the same quality of fit (DRMS = 0.63) as the MLR potential, but require many more parameters to do so.

For comparison, I've plotted the Dunham and MLR potentials together in Fig. 4.6. Differences in the two models can be seen easily. The MLR X0 potential is noticeably more narrow and complex than the Dunham one. The MLR B0 potential is slightly broader and $r_{eq}$ is slightly larger than predicted by the Dunham potential. To further characterize the differences between the two, another useful comparison is to look at the fit residuals. With about three times as many parameters, the Dunham potential matches the MLR potential in terms of DRMS, but a plot of all the points $\Delta f/\sigma_f$[5] vs. rotational quantum number $J$ reveals another problem. As seen in Fig. 4.7, the fit residuals from the MLR potential are random, but those for the Dunham potential

[5] $\Delta f/\sigma_f$ = (theoretical value minus experimental value) divided by experimental uncertainty.

| Parameter | Base Value | Multiplier | Comment |
|---|---|---|---|
| $\rho_{ab}$ | 0.80 | 1 | from the damping function equation |
| $C_5$ | 2.638317 | $10^5$ | from Ref. [78] |
| $C_7$ | 2.17709 | $10^7$ | from Ref. [78] |
| $C_9$ | 3.525446 | $10^9$ | from Ref. [78] |
| $\mathcal{D}_e$ | 3.14531±0.002 | $10^3$ | dissociation energy for B0 state |
| $r_{eq}$ | 2.8987146±0.0000001 | 1 | equilibrium internuclear distance for B0 state |
| $p$ | 5 | 1 | chosen parameter |
| $q$ | 3 | 1 | chosen parameter |
| $r_{ref}$ | 3.00 | 1 | chosen reference internuclear distance |
| $\beta_0$ | 2.772417038632 | 1 | fit parameters for MLR potential |
| $\beta_1$ | 3.146180770997 | 10 | ⋮ |
| $\beta_2$ | 3.816937254598 | 10 | |
| $\beta_3$ | -6.168498337840 | $10^2$ | |
| $\beta_4$ | 8.400892893258 | $10^2$ | |
| $\beta_5$ | 2.854561309630 | $10^4$ | |
| $\beta_6$ | 8.352270339485 | $10^4$ | |
| $\beta_7$ | 5.521153228674 | $10^4$ | |
| $\beta_8$ | 5.326056000287 | $10^4$ | |

Table 4.2: MLR Parameters for $^{130}Te_2$ B0 state. All lengths are Å, all energies are $cm^{-1}$, and all $\beta_i$ are dimensionless.

X0 Constants

| v | $T_v$ | $B_v$ | $-D_v$ | $H_v$ | $L_v$ | $M_v$ | $N_v$ | $0_v$ |
|---|---|---|---|---|---|---|---|---|
| 0 | 0 | 0.0396226484 | -4.0972864×10$^{-09}$ | -2.5729459×10$^{-16}$ | -9.9969883×10$^{-23}$ | -5.8736361×10$^{-29}$ | -3.5850335×10$^{-35}$ | 3.9191729×10$^{-41}$ |
| 1 | 246.0211 | 0.0395229557 | -4.1082147×10$^{-09}$ | -2.6844209×10$^{-16}$ | -1.0711617×10$^{-22}$ | -2.4638806×10$^{-29}$ | -1.1404544×10$^{-35}$ | -5.4804449×10$^{-41}$ |
| 2 | 491.0014 | 0.0394228146 | -4.1196157×10$^{-09}$ | -2.7415895×10$^{-16}$ | -1.1080754×10$^{-22}$ | -2.2927785×10$^{-29}$ | -3.7884916×10$^{-37}$ | -1.4211271×10$^{-40}$ |
| 3 | 734.9348 | 0.0393223887 | -4.1312608×10$^{-09}$ | -2.7775815×10$^{-16}$ | -1.1277263×10$^{-22}$ | -5.0970269×10$^{-29}$ | -1.3565986×10$^{-37}$ | -2.2156743×10$^{-40}$ |
| 4 | 977.8186 | 0.0392217674 | -4.1430540×10$^{-09}$ | -2.8229988×10$^{-16}$ | -1.1434702×10$^{-22}$ | -1.0597658×10$^{-28}$ | -6.8529147×10$^{-36}$ | -2.8449330×10$^{-40}$ |
| 5 | 1219.6515 | 0.0391209704 | -4.1550103×10$^{-09}$ | -2.9057304×10$^{-16}$ | -1.1638551×10$^{-22}$ | -1.8467345×10$^{-28}$ | -1.8359212×10$^{-35}$ | -3.4516583×10$^{-40}$ |
| 6 | 1460.4321 | 0.0390199523 | -4.1672307×10$^{-09}$ | -3.0507867×10$^{-16}$ | -1.1936622×10$^{-22}$ | -2.8373602×10$^{-28}$ | -3.2773350×10$^{-35}$ | -3.8320090×10$^{-40}$ |
| 7 | 1700.1582 | 0.0389186082 | -4.1798806×10$^{-09}$ | -3.2801046×10$^{-16}$ | -1.2344976×10$^{-22}$ | -3.9942576×10$^{-28}$ | -5.1525491×10$^{-35}$ | -4.0141131×10$^{-40}$ |

B0 Constants

| v | $T_v$ | $B_v$ | $-D_v$ | $H_v$ | $L_v$ | $M_v$ | $N_v$ | $0_v$ |
|---|---|---|---|---|---|---|---|---|
| 0 | 22876.8837 | 0.0310385929 | -4.7745502×10$^{-09}$ | 6.6641307×10$^{-15}$ | -1.4221889×10$^{-20}$ | 1.2185071×10$^{-26}$ | 7.5284690×10$^{-32}$ | -5.6674635×10$^{-37}$ |
| 1 | 23035.2376 | 0.0312972295 | -5.1235276×10$^{-09}$ | 3.3699164×10$^{-15}$ | 2.7436287×10$^{-21}$ | -2.985682×10$^{-26}$ | 4.7788517×10$^{-33}$ | 5.7607025×10$^{-37}$ |
| 2 | 23191.9613 | 0.0314604918 | -5.1032883×10$^{-09}$ | 8.2479496×10$^{-16}$ | 2.1271328×10$^{-21}$ | 8.4059858×10$^{-27}$ | -9.8762960×10$^{-32}$ | 7.6945537×10$^{-38}$ |
| 3 | 23348.8558 | 0.0315549499 | -5.1142714×10$^{-09}$ | -8.9830122×10$^{-17}$ | -2.5252153×10$^{-21}$ | 1.1476523×10$^{-26}$ | -2.8765559×10$^{-33}$ | -2.3211019×10$^{-37}$ |
| 4 | 23506.011 | 0.0316048245 | -5.2492819×10$^{-09}$ | -4.7595663×10$^{-16}$ | -4.3877151×10$^{-21}$ | -3.6439525×10$^{-27}$ | 6.1576331×10$^{-32}$ | -2.8652266×10$^{-37}$ |
| 5 | 23662.94 | 0.0316228383 | -5.4829508×10$^{-09}$ | -1.0187900×10$^{-15}$ | -3.0243996×10$^{-21}$ | -2.6847904×10$^{-26}$ | 1.199511×10$^{-31}$ | -3.1464249×10$^{-37}$ |
| 6 | 23819.0679 | 0.0316135943 | -5.7610053×10$^{-09}$ | -2.1256276×10$^{-15}$ | 1.7380909×10$^{-21}$ | -5.3688326×10$^{-26}$ | 1.3762175×10$^{-31}$ | 8.4849065×10$^{-38}$ |
| 7 | 23973.9146 | 0.0315765494 | -6.0188271×10$^{-09}$ | -4.0324180×10$^{-15}$ | 9.083824×10$^{-21}$ | -6.7221258×10$^{-26}$ | 1.5015506×10$^{-32}$ | 1.1342619×10$^{-36}$ |
| 8 | 24127.1576 | 0.0315082334 | -6.1950981×10$^{-09}$ | -6.6588575×10$^{-15}$ | 1.5882875×10$^{-20}$ | -4.1161099×10$^{-26}$ | -2.6558433×10$^{-31}$ | 1.8598337×10$^{-36}$ |
| 9 | 24278.6322 | 0.0314046510 | -6.2517698×10$^{-09}$ | -9.4757887×10$^{-15}$ | 1.7777653×10$^{-20}$ | 3.1327690×10$^{-26}$ | -4.7644327×10$^{-31}$ | 5.7891142×10$^{-37}$ |
| 10 | 24428.2909 | 0.0312638509 | -6.1870836×10$^{-09}$ | -1.1673829×10$^{-14}$ | 1.2891352×10$^{-20}$ | 1.1408231×10$^{-25}$ | -3.4016221×10$^{-31}$ | -2.2331834×10$^{-36}$ |
| 11 | 24576.1481 | 0.0310877240 | -6.0278591×10$^{-09}$ | -1.2624143×10$^{-14}$ | 3.7071865×10$^{-21}$ | 1.5270063×10$^{-25}$ | 4.5830643×10$^{-32}$ | -3.8700043×10$^{-36}$ |
| 12 | 24722.2412 | 0.0308821009 | -5.8095623×10$^{-09}$ | -1.2265574×10$^{-14}$ | -6.0789172×10$^{-21}$ | 1.2004438×10$^{-25}$ | 2.7255172×10$^{-31}$ | -3.2762029×10$^{-36}$ |

Table 4.3: Improved Dunham parameters for $^{130}Te_2$ X0 and B0 states.

All units are cm$^{-1}$.

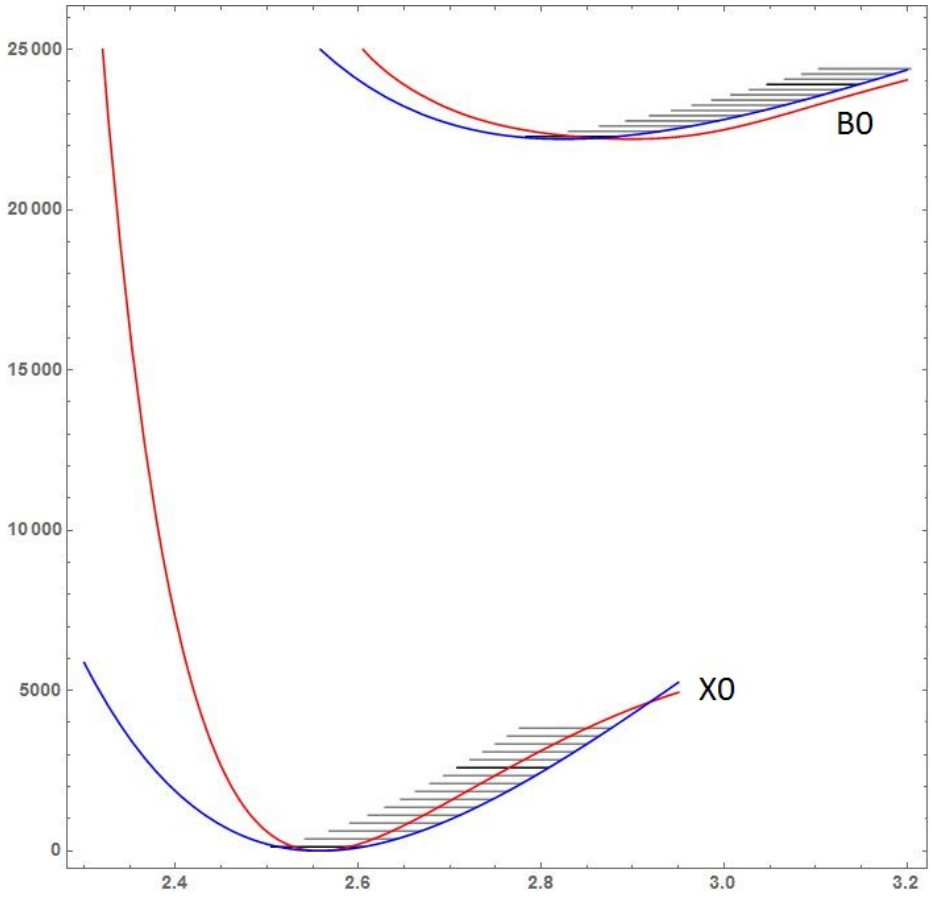


Figure 4.6: Comparison of Dunham (blue) and MLR (red) potentials vs. internuclear distance ($cm^{-1}$ vs Å)

exhibit polynomial patterns. This was done for several vibrational bands and similar patterns vs. randomness was always seen, but in Fig. 4.7 I've just shown one example. When any fit residuals exhibit a pattern, it is a clear indication that the model is incorrect. The random fit residuals, of course, merely indicate noise in the data.

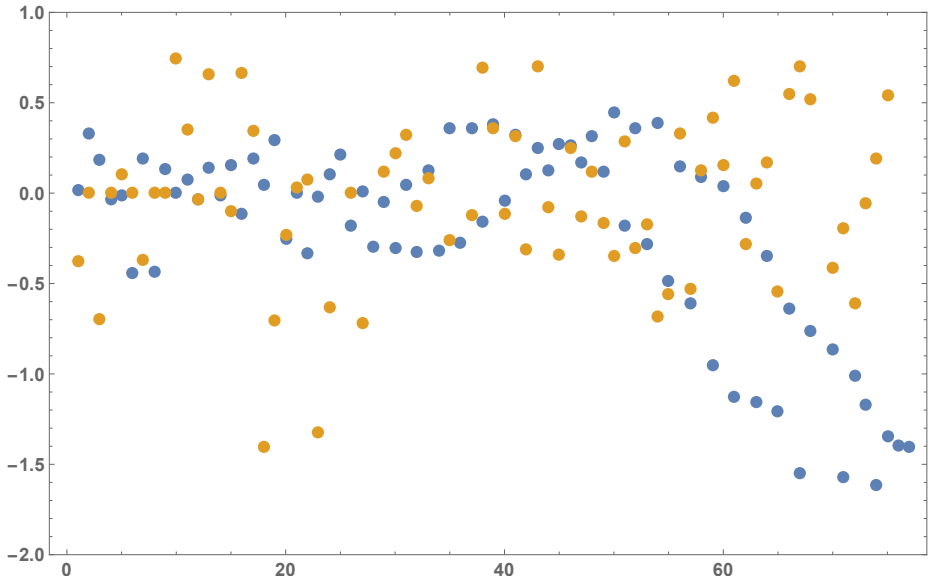


Figure 4.7: Comparison of Dunham (blue) and MLR (yellow) fit residuals ($\Delta f/\sigma_f$ vs rotational quantum number $J$). In this example we are looking at the X0($v' = 5$)←B0($v = 8$) vibrational band.

Finally, looking at the value for $\chi^2$ confirms those statements. For the MLR potential fitting, 11 parameters were used and $\chi^2 = 0.815$. This would suggest that the overal uncertainty should actually be about 90.3% of the value we used. Under the Dunham model, there are many different choices available for number of parameters, and it may not be clear how many parameters should be used. For this reason, I've explored several different options and the $\chi^2$ value for each. It appears that $\chi^2$ is a minimum when 112 parameters are used (7 for each vibrational band). Increasing the

| Terms Included | Number of Terms | $\chi^2$ |
|---|---|---|
| $T_v$ | 16 | $7.79 \times 10^9$ |
| $... + B_v$ | 32 | $8.47 \times 10^5$ |
| $... - D_v$ | 48 | $3.35 \times 10^4$ |
| $... + H_v$ | 64 | 494 |
| $... + L_v$ | 80 | 1.74 |
| $... + M_v$ | 96 | 1.66 |
| $... + N_v$ | 112 | 1.07 |
| $... + O_v$ | 128 | 1.11 |

Table 4.4: $\chi^2$ values for Dunham potential fits

number of parameters steadily increases $\chi^2$.

## 4.5 Conclusion

Starting with 1400 assigned $^{130}Te_2$ lines, we faced the task of characterizing the molecule to improved precision over those that did this in the past. We successfully characterized the ground state to a precision greater than that of Ref. [73] but require only a third as many parameters. We also characterized the B0 state in a novel way. The MLR potential provides a useful method for describing diatomic potentials with few parameters. It has also been shown that it can be extrapolated quite far beyond the range of the data used to create the function [21]. This is a great improvement over the classic Dunham model. We also have measured the Dunham constants for

$^{130}Te_2$ to a few orders of magnitude better than what had been done before.

Although the MLR potential can be extracted quite far, the data we present only goes to vibrational levels of $v = 15$ or so, but from Fig. 4.3 we can see that the ground state goes well past $v = 70$ before reaching dissociation. Thus it would be very helpful to obtain some more line-assigned $^{130}Te_2$ data for very high vibrational states to get the full potential.

Initially when assigning lines, preliminary values for the Dunham constants were obtained from Refs. [72, 73]. It is possible that with these new, more precise Dunham constants, we may be able to match a few hundred more lines, particularly in vibrational bands coming from the ground-state (X0) $v' = 0'$. Previously we weren't able to match any of those, but with these new constants another check might be worthwhile. That in turn could lead to an improved MLR potential, and the process could go on iteratively until we've assigned a significant fraction of the 9000 lines. While this would refine our $^{130}Te_2$ potential somewhat, we would still need some higher ($v \geq 70$) vibrational bands to complete the model.

I would like to thank Nikesh Dattani for useful conversations and contributions to analysis.

## Chapter 5

# Conclusion

These four experiments are different and interest different groups of people. The studies of Nitric Oxide interest a wide variety of scientists because of NO's important in nature. The disperion tuning spectroscopy experiment would be of interest to those taht need a laser system that can scan short distances very precisely. The more advanced laser system including many locks and a more detailed analysis of the data would be of interest to those needing a system that can scan over hundreds of GHz. Finally, the spectroscopic study of $^{130}Te_2$ is of interest to chemists and spectroscopists that are focused on heavy diatmoics. The common thread among all these experiments is diatomic molecules, and I've shown various applications for them.

In the Nitric Oxide experiment, the analytical and experimental groundwork was setup for trappic NO. Dahal's focus was more on the permanent magnet setup itself [10], and carrying out the optical pumping. This work focused on theory behind optical pumping, and experimentally demonstrating a working spectroscopy system. At the time I left the experiment, we had about 35 mW of power in the optical pumping beam (226 nm), but it was in a lab across the hall from the lab which contained the NO setup. We set up mirrors and PVC pipes and even drilled holes in the wall to port the 226 beam from one lab to the other, but unfortunately the loss of power was too great. The power of the 226 nm beam in the NO lab was less than 1 mW, so we were unable to demonstrate the population shift from $^2\Pi_{1/2}(v = 0)$ to $^2\Pi_{1/2}(v = 1)$. From

that point I begun work on setting up the tellurium cell while P. Dahal continued the NO experiment. In the end, my part was essentially creating the ultraviolet light source and setting up a working NO spectroscopy system. I took data with that system and matched a few dozen transitions, thus calibrating our laser.

Cavity dispersion tuning (CDT) was a success and we published the results in *The Journal for the Optical Society of America B*, as shown above. CDT spectroscopy is fairly easy to implement, quite accurate, and very reliable for short scans. Anyone requiring a stable and precise laser system that only needs to scan 1 GHz or less could make use of it.

The third experiment (Sec. 3.4), and further improvements to our laser system, was also a success. The new locking mechanisms were stable over several months. The way we stabilized our cavity's temperature and length yet maintained tunability could be a boon to anyone making precision measurements. Highly stabilized optical cavities have been done before to better precision [80, 81], but typically that work was done for optical clocks or other experiments where scanning is not required. Frequeny combs [64] are capable of both, but as of the date of this work, they are considerably expensive. Our system of highly stable layered locks and frequency 'markers' is less of a financial burden and yields similar results.

The final experiment was to take our atlas of $^{130}Te_2$ data and start assigning lines for improvement of spectroscopic parameters. This involved tens of thousands of lines of code in Mathematica as well as software developed in C++ [79]. In the end we succeeded in improving the Dunham parameters by a few orders of magnitude as

well as characterizing the the molecule with the new MLR potential [18]. Though we successfully measured these parameters, we found that measurement of a few of $^{130}Te_2$'s high vibrational bands (perhaps $v > 50$) would improve the result and possibly yield the full potential. This potential can be extrapolated quite far and can be used to match more transitions. Those interested in spectroscopy of heavy diatomics would be interested in this work.

Precision diatomic spectroscopy is a field that brings physicists and chemists together for a wide variety of studies. My hope is that these studies of nitric oxide and tellurium are found useful for others. I'd like to thank all the great people I worked with in and out of lab, such as Chris McRaven, Milinda Rupasinghe, Tao Yang, Jeffrey Gillean, Jacob Stinnet, and Parshuram Dahal. Most of all, I'd like to thank my advisors Neil Shafer-Ray and John Moore-Furneaux. I will carry their words and experience with me the rest of my life.

# References


[1] V. Flambaum and M. Kozlov, Physical review letters **99**, 150801 (2007).

[2] J. Hudson, B. Sauer, M. Tarbutt, and E. Hinds, Physical review letters **89**, 023003 (2002).

[3] M. Kozlov and L. Labzowsky, Journal of Physics B: Atomic, Molecular and Optical Physics **28**, 1933 (1995).

[4] D. Petrov, C. Salomon, and G. Shlyapnikov, Journal of Physics B: Atomic, Molecular and Optical Physics **38**, S645 (2005).

[5] R. M. Palmer, A. Ferrige, and S. Moncada, (1987).

[6] W. C. Sessa, Journal of vascular research **31**, 131 (1994).

[7] G. L. Squadrito and W. A. Pryor, Free Radical Biology and Medicine **25**, 392 (1998).

[8] G. Chung, C. Tin, J. Williams, K. McDonald, M. Di Ventra, S. Pantelides, L. Feldman, and R. Weller, Applied Physics Letters **76**, 1713 (2000).

[9] A. Bouwman, Nature **392**, 866 (1998).

[10] P. Dahal, *Progress towards producing and trapping cold nitric oxide* (University of Oklahoma, Norman, OK, 2012).

[11] M. E. Weeks, Journal of Chemical Education **12**, 403 (1935).

[12] K. W. FRANKE and A. L. MOXON, Journal of Pharmacology and Experimental Therapeutics **58**, 454 (1936).

[13] J. Cariou and P. Luc, in *Atlas du spectre d'absorption de la molecule de tellure, 21800-22908* (Laboratoire Aime-Cotton, Orsay, France, 1980), p. 23.

[14] M. Roberts, P. Taylor, G. Barwood, W. Rowley, and P. Gill, Physical Review A **62**, 020501 (2000).

[15] D. McIntyre, W. Fairbank Jr, S. Lee, T. Hänsch, and E. Riis, Physical Review A **41**, 4632 (1990).

[16] G. Barwood, W. Rowley, P. Gill, J. Flowers, and B. Petley, Physical Review A **43**, 4783 (1991).

[17] E. R. Peck and B. N. Khanna, J. Opt. Soc. Am. **56**, 1059 (1966).

[18] R. J. Le Roy, N. S. Dattani, J. A. Coxon, A. J. Ross, P. Crozet, and C. Linton, The Journal of chemical physics **131**, 204309 (2009).

[19] J. Dunham, Physical Review **41**, 721 (1932).

[20] M. Semczuk, X. Li, W. Gunton, M. Haw, N. S. Dattani, J. Witz, A. K. Mills, D. J. Jones, and K. W. Madison, Physical Review A **87**, 052505 (2013).

[21] N. S. Dattani and R. J. Le Roy, Journal of Molecular Spectroscopy **268**, 199 (2011).

[22] D. DeMille, *Quantum Electronics and Laser Science Conference* (Yale University, Baltimore, Maryland, 2011).

[23] G. Quéméner and J. L. Bohn, Phys. Rev. A **83**, 012705 (2011).

[24] J. Deiglmayr, M. Repp, A. Grochola, O. Dulieu, R. Wester, and M. Weidemüller, Journal of Physics: Conference Series **264**, 012014 (2011).

[25] Q. Wei, S. Kais, B. Friedrich, and D. Herschbach, **134**, 124107 (2011).

[26] B. J. Bichsel, Ph.D. thesis, University of Oklahoma, Norman, Oklahoma, 2005.

[27] L. J. Ignarro, *Nitric Oxide: Biology and Pathobiology*, 2 ed. (Elsevier Science, UCLA, 2009).

[28] J. B. George B. Richter-Addo, Peter Legzdins, Chem. Rev. **102**, 857 (2002).

[29] G. Reiser, W. Habenicht, K. Mller-Dethlefs, and E. W. Schlag, Chemical Physics Letters **152**, 119 (1988).

[30] G. Herzberg, in *Molecular Spectra and Molecular Structure* (Prentice-Hall, Inc., New York, 1939).

[31] R. Engleman Jr, P. Rouse, H. Peek, and V. Baiamonte, Technical report, Los Alamos Scientific Lab., N. Mex. (unpublished).

[32] C. B. Collins, B. W. Johnson, M. Y. Mirza, D. Popescu, and I. Popescu, Phys. Rev. A **10**, 813 (1974).

[33] P. M. Johnson, The Journal of Chemical Physics **62**, 4562 (1975).

[34] H. Scheingraber and C. R. Vidal, J. Opt. Soc. Am. B **2**, 343 (1985).

[35] G. C. Bhar, P. Kumbhakar, U. Chatterjee, A. K. Chaudhary, and A. Kokh, Pramana Journal of Physics **59**, 69 (2002).

[36] R. W. Boyd, *Nonlinear Optics*, 2 ed. (Academic Press, Rochester, New York, 2003).

[37] S. Hooker and C. Webb, *Laser Physics* (Oxford University Press, Inc., New York, 2010).

[38] E. G. Marason, Optics Communications **37**, 56 (1981).

[39] J. Brown and A. Carrington, *Rotational spectroscopy of diatomic molecules*, *Cambridge molecular science series* (Cambridge University Press, Cambridge, UK, 2003).

[40] J. Danielak, U. Domin, R. Ke, M. Rytel, and M. Zachwieja, Journal of Molecular Spectroscopy **181**, 394 (1997).

[41] D. Turner and D. May, The Journal of Chemical Physics **45**, 471 (1966).

[42] R. Nicholls, Journal of Physics B: Atomic and Molecular Physics **1**, 1192 (1968).

[43] H. A. Ory, The Journal of Chemical Physics **40**, 562 (1964).

[44] N. E. Shafer-Ray, Physical Review A **73**, 034102 (2006).

[45] T. J. Scholl, S. J. Rehse, R. A. Holt, and S. D. Rosner, J. Opt. Soc. Am. B **22**, 1128 (2005).

[46] J. Coker, H. Fan, C. McRaven, P. Rupasinghe, T. Z. Yang, N. Shafer-Ray, and J. Furneaux, JOSA B **28**, 2934 (2011).

[47] R. N. Hall, G. E. Fenner, J. D. Kingsley, T. J. Soltys, and R. O. Carlson, Phys. Rev. Lett. **9**, 366 (1962).

[48] M. I. Nathan, W. P. Dumke, G. Burns, F. H. Dill, Jr., and G. Lasher, App. Phys. Lett. **1**, 62 (1962).

[49] C. Bradley, J. Chen, and R. G. Hulet, Rev. Sci. Instr. **61**, 2097 (1990).

[50] D. Wang, L. Xie, and Y. Wang, Opt. Lett. **13**, 820 (1988).

[51] K. L. Corwin, Z.-T. Lu, C. F. Hand, R. J. Epstein, and C. E. Wieman, Applied Optics **37**, 3295 (1998).

[52] J. H. T. Burke, O. Garcia, K. J. Hughes, B. Livedalen, and C. A. Sackett, Rev. Sci. Instr. **76**, 116105 (2005).

[53] U. Griesmann and J. Burnett, Opt. Lett. **24**, 1699 (1999).

[54] D. W. Allan, Proc. of the IEEE **54**, 221 (1966).

[55] A. Buckingham and C. Graham, Proc. R. Soc. Lond. A. **336**, 275 (1974).

[56] J. Old, K. Gentili, and E. Peck, J. Opt. Soc. Am. **61**, 89 (1971).

[57] E. D. Black, Am. J. Phys. **69**, 79 (2001).

[58] J. Baron, W. C. Campbell, D. DeMille, J. M. Doyle, G. Gabrielse, Y. V. Gurevich, P. W. Hess, N. R. Hutzler, E. Kirilov, I. Kozyryev, *et al.*, Science **343**, 269 (2014).

[59] E. Shuman, J. Barry, and D. DeMille, Nature **467**, 820 (2010).

[60] I. Barmes, S. Witte, and K. S. Eikema, Physical review letters **111**, 023007 (2013).

[61] J. Zhang, W. Yuan, K. Deng, A. Deng, Z. Xu, C. Qin, Z. Lu, and J. Luo, Review of Scientific Instruments **84**, 123109 (2013).

[62] D. Blume, Reports on Progress in Physics **75**, 046401 (2012).

[63] G. Bjorklund, M. Levenson, W. Lenth, and C. Ortiz, Applied Physics B **32**, 145 (1983).

[64] S. A. Diddams, D. J. Jones, J. Ye, S. T. Cundiff, J. L. Hall, J. K. Ranka, R. S. Windeler, R. Holzwarth, T. Udem, and T. Hänsch, Physical Review Letters **84**, 5102 (2000).

[65] D. J. Jones, S. A. Diddams, J. K. Ranka, A. Stentz, R. S. Windeler, J. L. Hall, and S. T. Cundiff, Science **288**, 635 (2000).

[66] J. D. Gillaspy and C. J. Sansonetti, J. Opt. Soc. Am. B **8**, 2414 (1991).

[67] J. I. Thorpe, K. Numata, and J. Livas, Optics express **16**, 15980 (2008).

[68] T. Udem, J. Reichert, R. Holzwarth, and T. Hänsch, Physical review letters **82**, 3568 (1999).

[69] F. Nix and D. MacNair, Physical Review **60**, 597 (1941).

[70] G. D. Boyd and J. P. Gordon, Bell System Technical Journal **40**, 489 (1961).

[71] P. Courteille, L. Ma, W. Neuhauser, and R. Blatt, Appl. Phys. B **59**, 187 (1994).

[72] K. Huber, G. Herzberg, J. Gallagher, and I. R.D. Johnson, *NIST Chemistry WebBook, Constants of Diatomic Molecules* (NIST Standard Reference Database, Gaithersburg, MD, 2015).

[73] J. Vergs, C. Effantin, O. Babaky, J. d'Incan, S. J. Prosser, and R. F. Barrow, Physica Scripta **25**, 338 (1982).

[74] W. J. Meath, American Journal of Physics **40**, (1972).

[75] J. O. Hirschfelder, C. F. Curtiss, and R. B. Bird, (Wiley, Hoboken, NJ, YEAR).

[76] R. J. Le Roy, C. C. Haugen, J. Tao, and H. Li, Molecular Physics **109**, 435 (2011).

[77] C. Douketis, G. Scoles, S. Marchetti, M. Zen, and A. Thakkar, The Journal of Chemical Physics **76**, 3057 (1982).

[78] A. Polo, J. Poyato, J. Camacho, and A. Pardo, Journal of Quantitative Spectroscopy and Radiative Transfer **60**, 989 (1998).

[79] R. L. Roy, Department of Chemistry Computer Programs DPotFit, 2013.

[80] J. McFerran, D. Magalhães, C. Mandache, J. Millo, W. Zhang, Y. Le Coq, G. Santarelli, and S. Bize, Optics letters **37**, 3477 (2012).

[81] Y. Luo, B. Ouyang, X. Zeng, A. Deng, C. Qin, K. Deng, J. Zhang, Z. Lu, and J. Luo, in *European Frequency and Time Forum & International Frequency Control Symposium (EFTF/IFC), 2013 Joint*, IEEE (Huazhong Univ. of Sci. & Technol., ADDRESS, 2013), pp. 385–387.